

Origami concave tubes for energy absorption

Yang Li^{a,*}, Zhong You^b

^a Graduate Aerospace Laboratories, California Institute of Technology, 1200 E. California Blvd., Pasadena CA 91125, USA

^b Department of Engineering Science, University of Oxford, Parks Road, Oxford, OX1 3PJ, UK



ARTICLE INFO

Article history:

Received 29 October 2018

Revised 14 February 2019

Accepted 21 March 2019

Available online 22 March 2019

Keywords:

Energy absorption

Thin-walled structures

Concave cross-sections

Origami

ABSTRACT

The paper investigates the energy absorption performance of a new type of thin-walled tubes named as *origami concave tubes* whose cross-sections are concave polygons. Through the introduction of origami initiators, a reliable and progressive buckling failure mode can be successfully triggered, which is not a common feature for tubes with concave cross-sections. These origami concave tubes can achieve ultra-high energy absorption capability accompanied with relatively low peak forces. A comprehensive numerical, experimental, and theoretical analysis has been performed which shows that origami concave tubes can achieve 3.3 times the specific energy absorption of the comparable square tubes. We have also illustrated that origami concave tubes are approaching the theoretical limit of energy absorption.

© 2019 Published by Elsevier Ltd.

1. Introduction

A significant amount of research has been done on the energy absorption of stocky thin-walled tubes when subjected to axial compression. It has been well understood that, under axial compression, a thin-walled square tube made from ductile materials can have a progressive buckling mode (DiPaolo and Tom, 2006), which is a preferable feature for energy absorbers to have (Lu and Yu, 2003). It is also known that the corners of a square tube made from ductile materials absorb two-thirds of the energy under the crushing process because of the formation of travelling hinges (Wierzbicki and Abramowicz, 1983; Ma and You, 2013). In consequence, energy absorption might be enhanced by increasing the number of corners of the tube, which prompted researchers to focus on other multi-corner thin-walled tubes with cross-sections of both convex and concave polygons (Fan et al., 2013; Tang et al., 2012; Liu et al., 2015; Reddy et al., 2015; Deng et al., 2018; Liu et al., 2016).

Mathematically, a concave cross-section is a polygonal shape of at least one reflex interior angle (Weisstein). Concave cross-sections can unlimitedly increase the number of corners while convex cross-sections become effectively circular when there is a large number of "corners". This indicates that tubes with concave cross-sections have potential for ultra-high energy absorption. In the past, a number of tubes with concave cross-sections have been studied (Fan et al., 2013; Deng et al., 2018; Liu et al., 2016). Though

numerical simulations with specific settings have shown the possibility of the progressive buckling for tubes with concave cross-sections (Tang et al., 2012; Reddy et al., 2015), this turned out to be not the case in reality. Experimental results of crushing tubes with various concave cross-sections can be found in (Fan et al., 2013; Deng et al., 2018; Liu et al., 2016), in which the tubes seemed to buckle in an irregular way where the surfaces bulge out or sway laterally, instead of buckling progressively. This performance results in high peak force and comparable energy absorption to circular tubes (Fan et al., 2013). A solution to successfully trigger the progressive buckling failure mode for thin-walled concave tubes, where ultra-high energy absorption is expected, has yet to be found.

There are three fundamental conditions for ultra-high energy absorption to occur. The first condition is the presence of a compatible failure mode that is inherent in the tube, and that mode corresponds to a high mean crush force which leads to high energy absorption. The second condition is that the tube itself should have an ultra-high buckling force which is significantly larger than the mean crush force, otherwise the tube will fail due to instability instead of deforming according to the target failure mode. The third condition is the presence of an "initiator" that lowers down the threshold of that particular failure mode (if needed). Tubes with concave cross-sections satisfy the first two conditions because they can have a large number of corners (high energy absorbing failure modes) and ultra-high buckling forces (Ning and Pellegrino, 2015; Li and You, 2018). However, the initiator is missing and the design of it is not trivial. Concave cross-sections with more corners have more kinematical freedom than convex cross-sections, so their surfaces are more likely to bulge out or sway laterally when com-

* Corresponding author.

E-mail address: chineseguyliyang@gmail.com (Y. Li).

pressed (Fan et al., 2013; Deng et al., 2018; Liu et al., 2016). In consequence, additional to triggering the target failure mode, the design of initiator shall retain the high buckling force of the tube as well as the stability of the shape of cross-section in the crushing process.

This paper proposes a new type of thin-walled tubes known as *origami concave tubes* that satisfy the above conditions. They have concave polygons as cross-sections and one layer of origami folding in one end of tubes as the initiator. A reliable and progressive buckling failure mode can be successfully triggered when compressed axially. This mode is associated with a relatively high energy absorption capability and low initial peak force. The paper is organized as follows. Section 2 presents the design of the concave origami tubes. Experiments and numerical simulations via Abaqus/Explicit (Abaqus, 2013) concerning crushing a square tube, normal concave tubes, and origami versions of concave tubes are given in Section 3. Section 4 presents the theoretical modelling of the mean crush forces of the origami concave tubes, which are then compared with numerical simulation results for validation. The parametric study using numerical simulations is given in Section 5. Section 6 provides the discussion of dynamic and inclined loading effects using the numerical simulations. Finally, Section 7 concludes the paper.

2. Geometry of origami concave tubes

Two concave tubes are shown in Fig. 1(a), (b), (d), and (e) respectively. One of the ends of each tube is slightly bent to create an origami initiator, which can be seen in Fig. 1(c) and (f) respectively. They are manufactured from a single sheet of metal using the origami patterns given in Fig. 2, which consist of a set of mountain (solid line) and valley creases (dash line). These are rigid origami patterns, i.e., continuous folding can be carried out by folding along the creases without stretching the sheet. Concave tubes can be obtained once edges AB meets A'B' and BC meets B'C'. It is expected that the increase in the number of corners will lead to failure modes with higher energy absorption capabilities. The geometry of origami concave tubes is determined by five independent parameters. They are: α , the pattern angle; l_1 , the length of the straight part of the tube; l_2 , the length of the inclined part; w , the width of an edge; and t , the wall thickness of the sheet, all of which are noted in Fig. 2.

Tubes with the shape shown in Fig. 1(b) will be denoted as O1 concave tubes (O1 stands for order 1), and the corresponding tubes in Fig. 1(c) will be denoted as O1 origami concave tubes. Similarly, the tubes shown in Fig. 1(e) and (f) will be denoted as O2 concave tubes and O2 origami concave tubes, respectively.

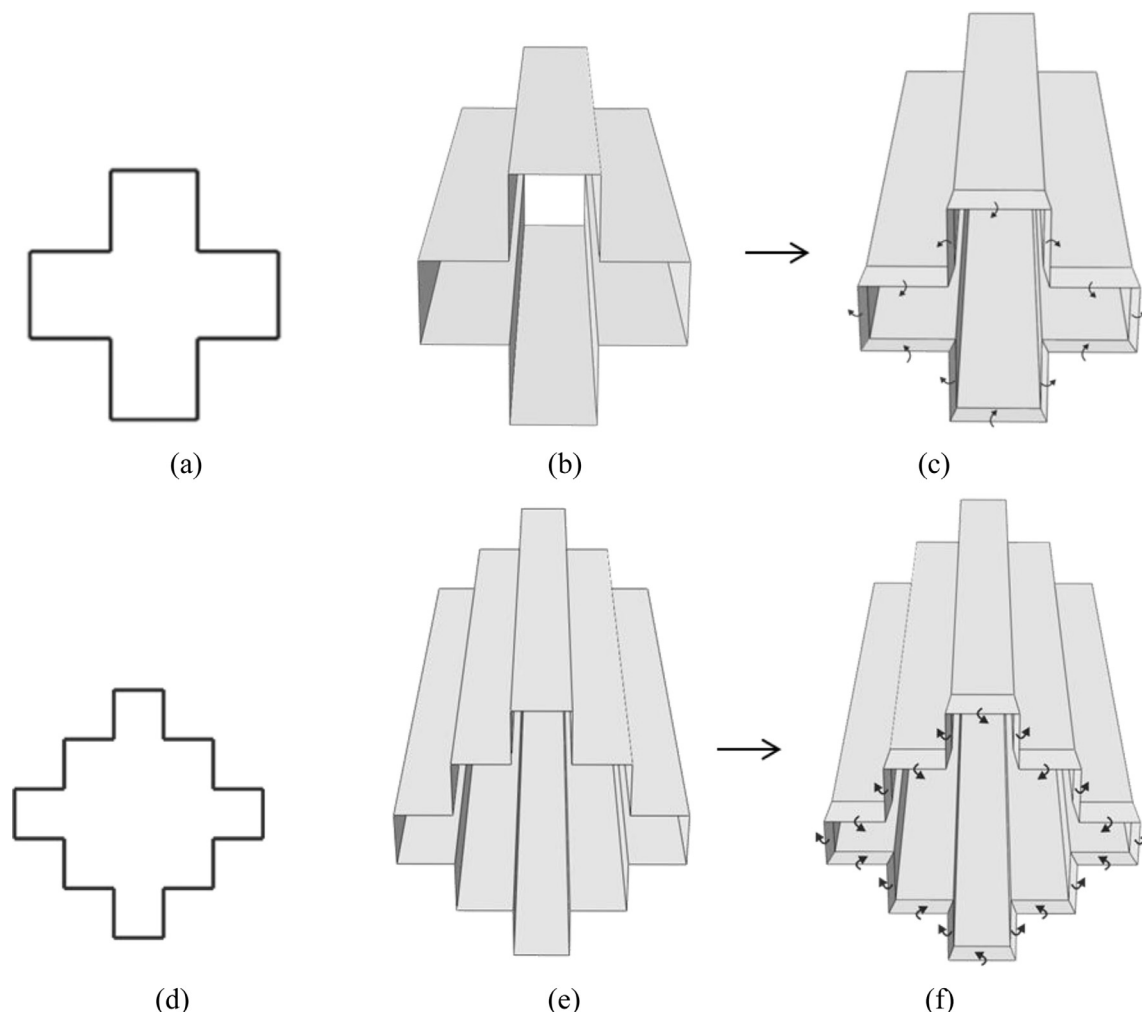


Fig. 1. Method used for generating origami concave tubes: (a) cross-section of one concave shape; (b) tube with the cross-section shown in (a); (c) origami initiator added to tube in (b); (d) cross-section of another concave shape; (e) tube with the cross-section in (d); and (f) origami initiator added to tube in (e).

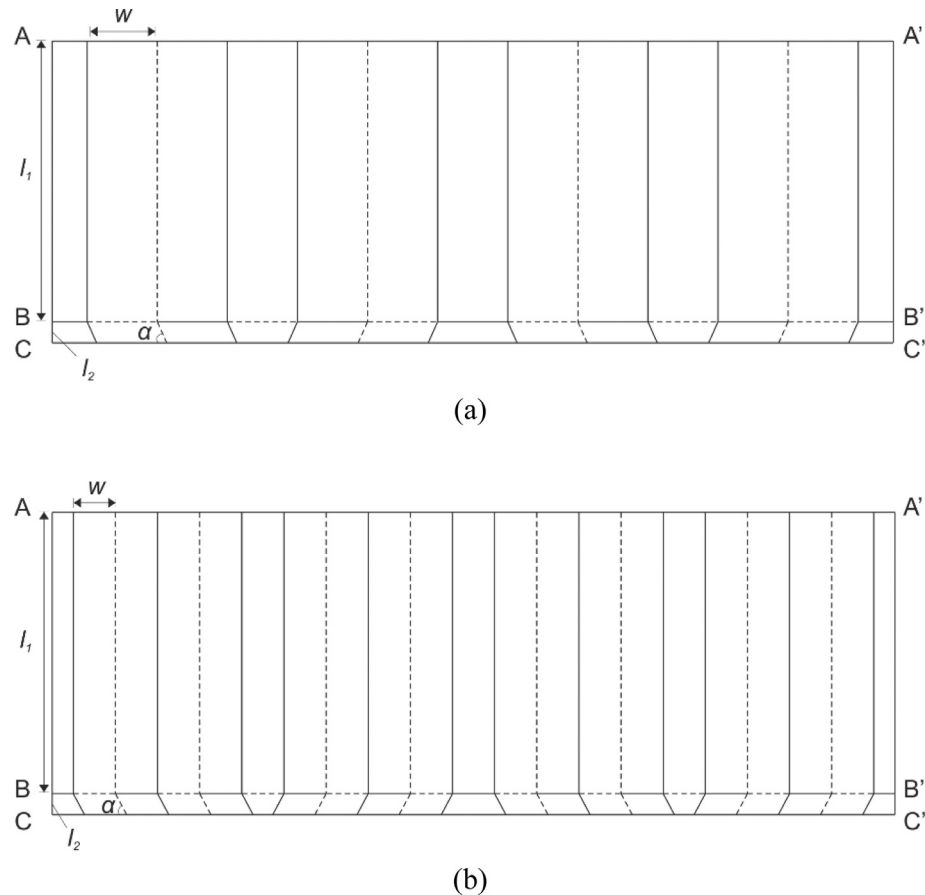


Fig. 2. Folding patterns for the (a) first and (b) second origami concave tubes seen in Fig. 1.

3. Experimental and numerical studies

3.1. Manufacturing and experiment setup

Five types of tubes were manufactured, i.e., the square tube, O1 concave tube, O1 origami concave tube, O2 concave tube, and O2 origami concave tube.

The dimensions of the cross-sections of the tubes are shown in Fig. 3. The total tube length was set as 150 mm. Each tube was spot welded from four smaller pieces with 15 mm overlaps, leaving the tube with four 15 mm thicker sections, which are marked in black in Fig. 3. All of the tubes were welded to two rigid plates by four tabs at each end, and the tabs were positioned at the overlapped and thicker part of tubes, as shown in Fig. 4. Parameters

Table 1
Parameters of the origami concave tubes.

Type	α (°)	l_1 (mm)	l_2 (mm)	w (mm)	t (mm)
O1 origami concave tube	80.66	142.5	7.5	25	0.9
O2 origami concave tube	80.66	142.5	7.5	15	0.9

for the prototypes are given in Table 1. The material used was a 304 stainless steel sheet. The dog-bone samples were cut from the sheet and tested. The material has density $\rho = 8030 \text{ kg/m}^3$, Young's modulus $E = 193 \text{ GPa}$, yield stress $\sigma_y = 241.3 \text{ N/mm}^2$, ultimate stress $\sigma_u = 679.6 \text{ N/mm}^2$, ultimate strain $\varepsilon_u = 55.8\%$, and strain hardening formula $\sigma = 1400\varepsilon^{0.44}$.

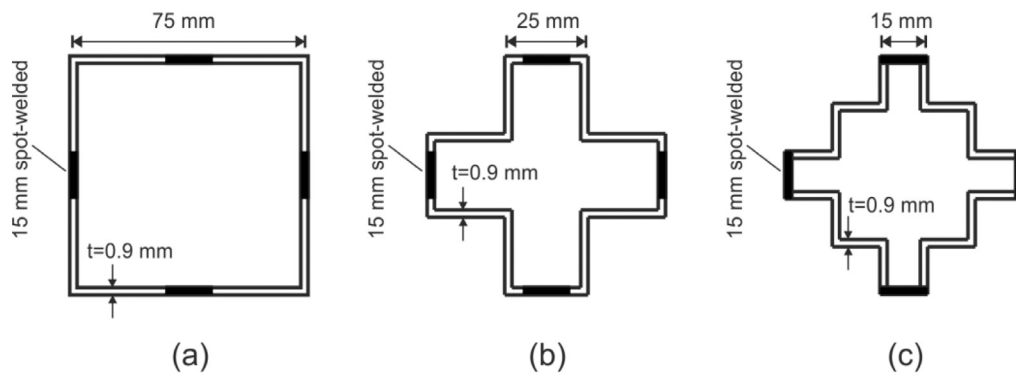


Fig. 3. Dimensions of the cross-sections of the tubes used in the experiment.

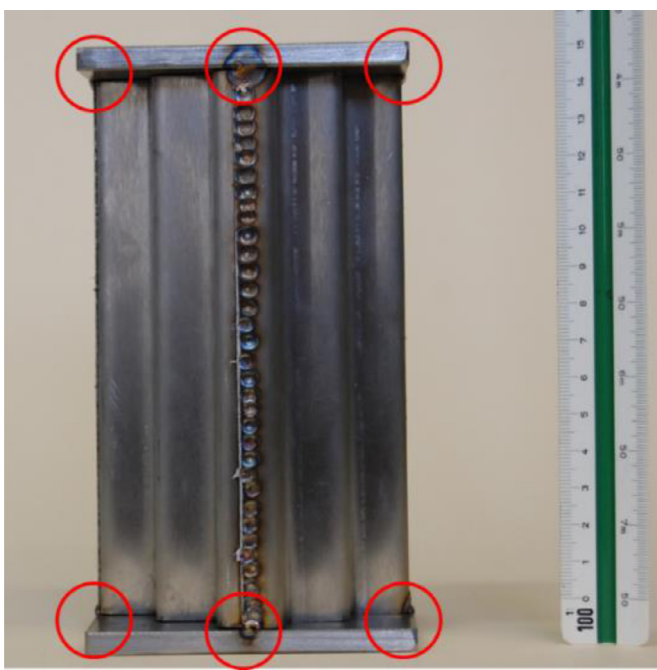
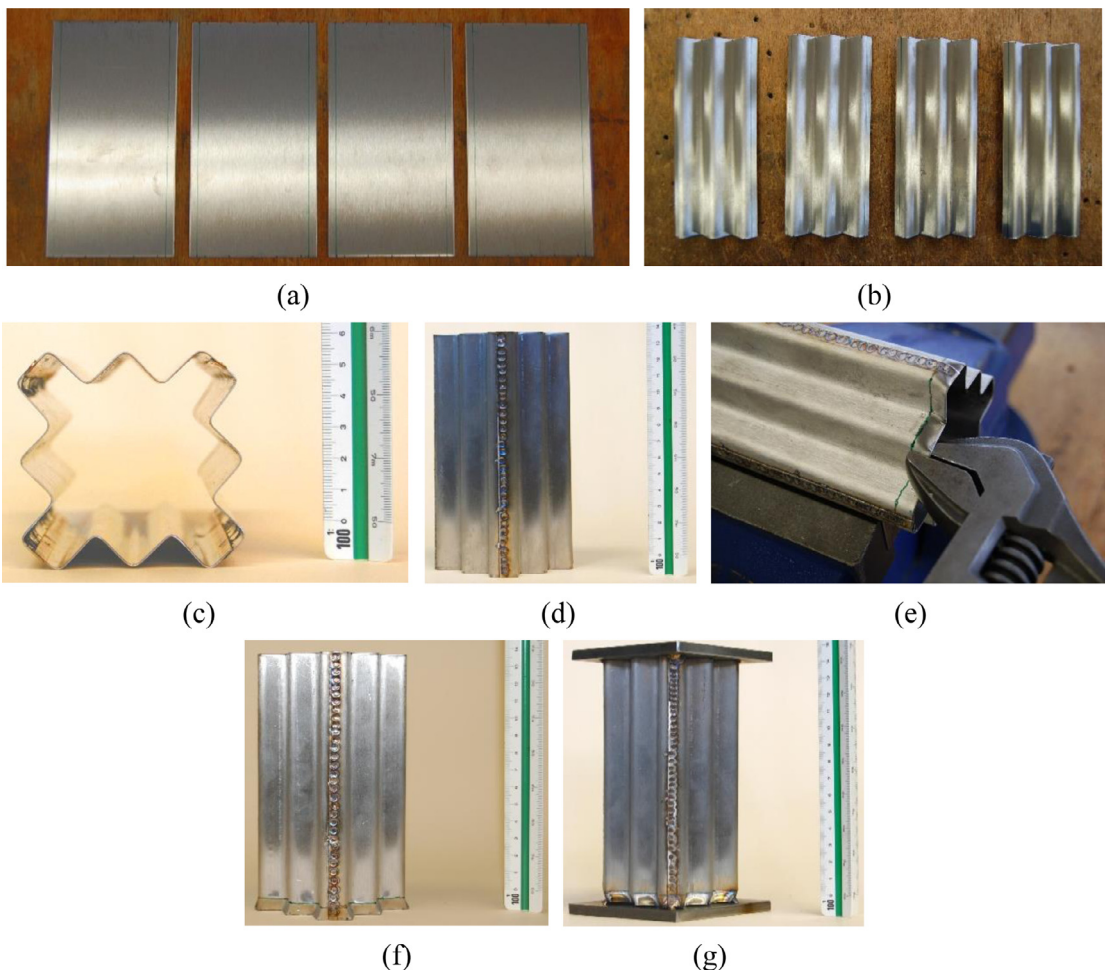


Fig. 4. Tube welded to end plates.



The tube prototypes were made with a series of bending and spot-welding processes. For example, for the O2 origami concave tube, four pieces of stainless steel were cut, and bent into a “w” shape, as shown in Fig. 5(a) and (b). Then the four w-shaped pieces were spot welded together, resulting in the concave tube shown in Fig. 5(c) and (d). After that, one end of the concave tube was bent manually with a spanner, forming the origami initiator seen in Fig. 5(e) and (f). Finally, the tube was welded to two steel plates with four 15 mm tabs at spot welded positions on each end, as shown in Fig. 5(g). The other tubes were made in a similar fashion, except that no origami initiator was made for the normal concave tubes. The material used has good ductility, and the residual stress from the manufacturing process was very small comparing to the stress experienced during the crushing process.

Three different testing methods were used because the buckling load of some specimens exceeded the limit of the load cell installed in the Instron machine available. Method 1 involved compressing the tube with an Instron 5982 set at a speed of 10 mm/min. Method 2 involved pre-buckling the tube via a hydraulic machine and then compressing it further via the Instron machine at a speed of 10 mm/min. Finally, Method 3 involved softening the specimen with annealing (heating to 1100 °C and quenching in oil for austenitic steel) and then compressing it via the Instron machine at a speed of 10 mm/min. The annealed 304 stainless steel was tested with dog-bone samples, and the stiffness and yield stress are both reduced significantly. In total, 13 spec-

Fig. 5. Manufacturing process for an O2 origami concave tube: (a) cut four pieces of material; (b) bend them into “w” shapes; (c) and (d) spot-weld four w-shaped pieces together and form the tube; (e) bend one end of the tube with a spanner to form the origami initiator; (f) a finished O2 origami concave tube; (g) the tube welded to two steel plates.

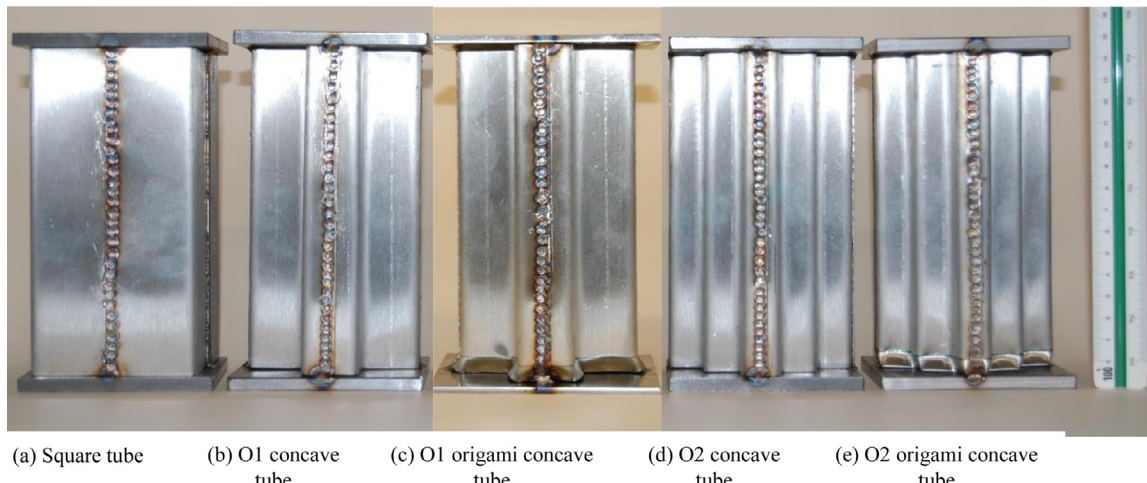


Fig. 6. Five types of tubes used in the experiment: (a) square tube, (b) O1 concave tube, (c) O1 origami concave tube, (d) O2 concave tube, and (e) O2 origami concave tube.

Table 2
Name and testing method for each specimen.

Specimen	Short Code	Testing Method	Material
Square tube	S1	1	304 stainless
O1 concave tube 1	O1C1	2	304 stainless
O1 concave tube 2	O1C2	1	304 stainless
O1 concave tube 3	O1C3	1	304 stainless
O1 origami concave tube 1	O1OC1	1	304 stainless
O1 origami concave tube 2	O1OC2	1	304 stainless
O1 origami concave tube 3	O1OC3	1	304 stainless
O2 concave tube 1	O2C1	2	304 stainless
O2 concave tube 2	O2C2	2	304 stainless
O2 concave tube 3	O2C3	3	Annealed 304 stainless
O2 origami concave tube 1	O2OC1	1	304 stainless
O2 origami concave tube 2	O2OC2	1	304 stainless
O2 origami concave tube 3	O2OC3	1	304 stainless

Table 3
Elements used for each numerical model.

Tube	Square	O1 concave	O1 origami concave	O2 concave	O2 origami concave
Elements	31,248 S4R	45,000 S4R	45,602 S4R	71,440 S4R	45,300 S4R

imens were prepared: 1 square tube, 3 O1 concave tubes, 3 O1 origami concave tubes, 3 O2 concave tubes, and 3 O2 origami concave tubes. All of which are shown in Fig. 6. The short codes for those specimens and the corresponding testing methods are listed in Table 2.

3.2. Numerical simulation setup

Abaqus/Explicit (Abaqus, 2013) was used for the numerical simulation. The number and types of elements used in the tubes are listed in Table 3. The tubes, as mentioned previously, were tied to two rigid plates at ends by four 15 mm length tabs, as illustrated in Fig. 7, which corresponds to the experimental setup. Each rigid plate used one R3D4 element. Superficial imperfections were added to the tubes by superposing the first buckling mode obtained through linear buckling analysis onto a perfect shape with an amplitude of 0.1 mm (Ning and Pellegrino, 2015), and this amplitude was validated with the experiment. The rigid plate at the bottom was fixed, and the one at the top one was controlled by displacement, moving down to a total of 120 mm in 0.1 s and generating an axial compression on the tubes. Convergence tests with respect to mesh density and analysis time were conducted prior to the analysis. These simulations can be regarded as quasi-static

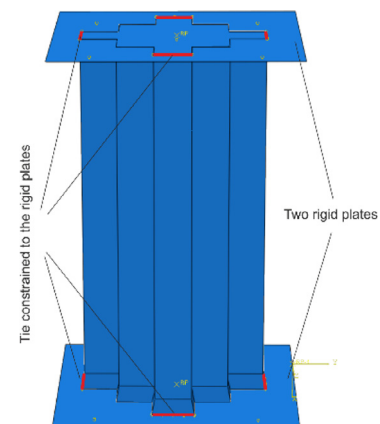


Fig. 7. Setup of numerical simulation.

processes since the kinematic energy was well below 5% of the internal energy (Abaqus, 2013). No hourglass deformation was observed visually throughout the simulation, and the consistency of the results was well maintained.

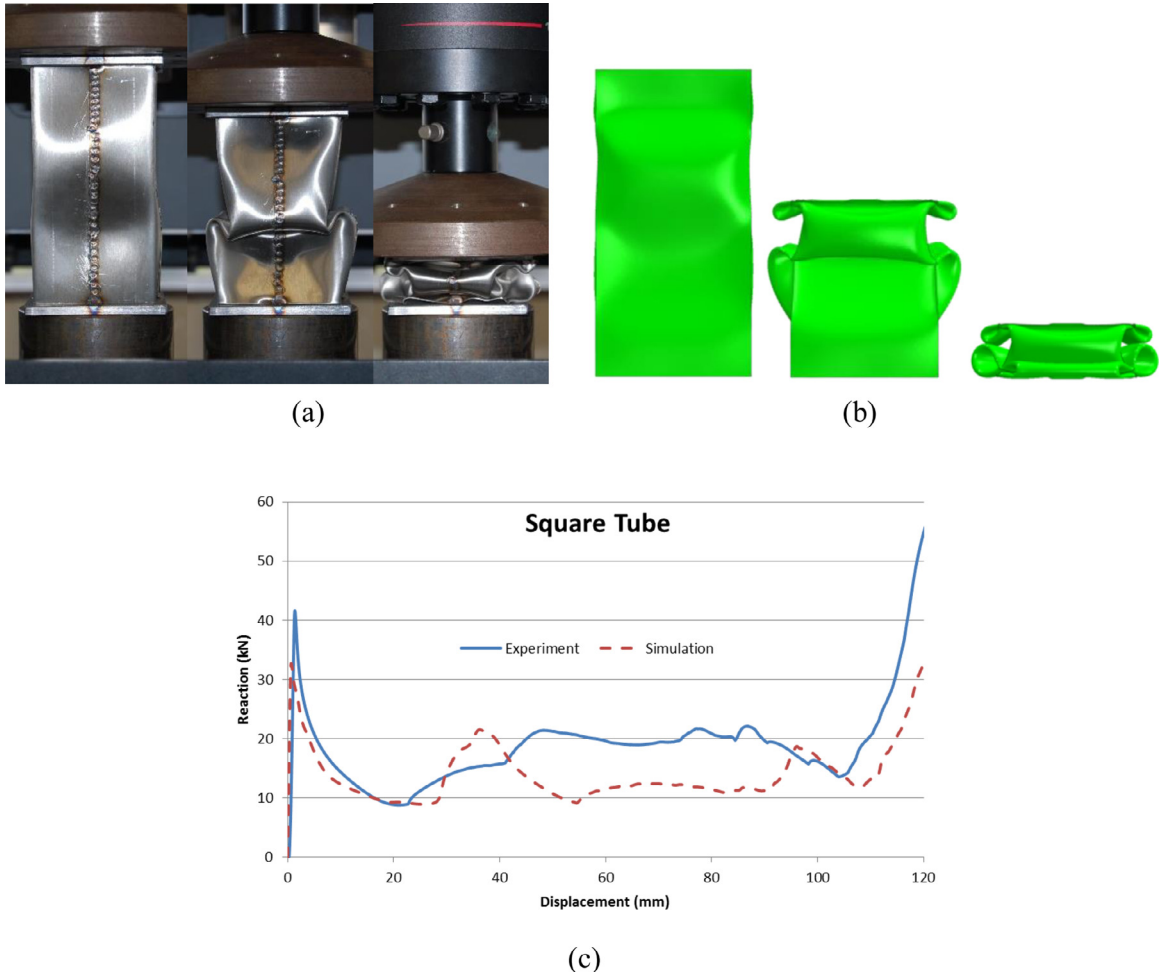


Fig. 8. Crushing the square tube with displacements of 2.4 mm, 60 mm, and 120 mm in (a) the experiment and (b) the simulation, plus (c) the reaction-displacement plots for the experiment and simulation.

3.3. Numerical and experimental results

Experiments were conducted on 13 tubes, and numerical simulations on 5 types of tubes were carried out. The deformation and reaction curves were collected and used for analyses and comparison.

3.3.1. Crushing of a square tube

The square tube was used as a benchmark. Fig. 8(a) and (b) show the typical experimental and numerical failure mechanisms of a square tube and indicate good consistency. The tube buckled and folded down into roughly three layers. The reaction-displacement plots for the experiment and simulation are given in Fig. 8(c), and a slight difference can be noticed in the post-buckling reactions.

3.3.2. Crushing of O1 concave tubes

The experimental crushing of O1C1 and O1C2 are presented in Fig. 9(a) and (b). Both of tubes swayed sideways and failed due to global instability, which differed from the progressive buckling mode demonstrated by the square tube. The third sample in the same group, O1C3, managed to buckle progressively, as shown in Fig. 9(c). It matched the results of the numerical simulation for the O1 concave tube (Fig. 9(d)), and both demonstrated a progressive buckling mode without capturing the instability problem. This

shows that the failure mode of O1 concave tubes is sensitive to the unsymmetrical imperfection in the experiment.

The reaction-displacement plots for the three experiments (O1C1, O1C2, and O1C3) and the simulation for the O1 concave tube is presented in Fig. 9(e). The differences in reaction responses between different failure modes are obvious. O1C1 and O1C2 showed identical responses, while the reactions of O1C3 and the numerical simulation were comparable to each other but significantly different from those of O1C1 and O1C2. A slight difference in the initial slopes of the reaction curves can be observed, which is due to small gaps and compliance within the structure and the loading system.

3.3.3. Crushing of O1 origami concave tubes

The compression of O1OC1 and numerical simulation of the crushing of the O1 origami concave tube demonstrated comparable progressive buckling modes, as shown in Fig. 10(a) and (b). Crushing O1OC2 and O1OC3 resulted in failure mechanisms that were identical to that of O1OC1. The reaction-displacement plots are shown in Fig. 10(c). The reaction curves for the three experiments were very close and showed small shifts and slightly lower initial slopes compared to that of the simulation. This shift was probably because the overlapped and spot-welded parts in the experimental samples were thicker and harder than the rest of the sample. In consequence, tubes folded by fewer layers in the experiments than they did in the simulation.

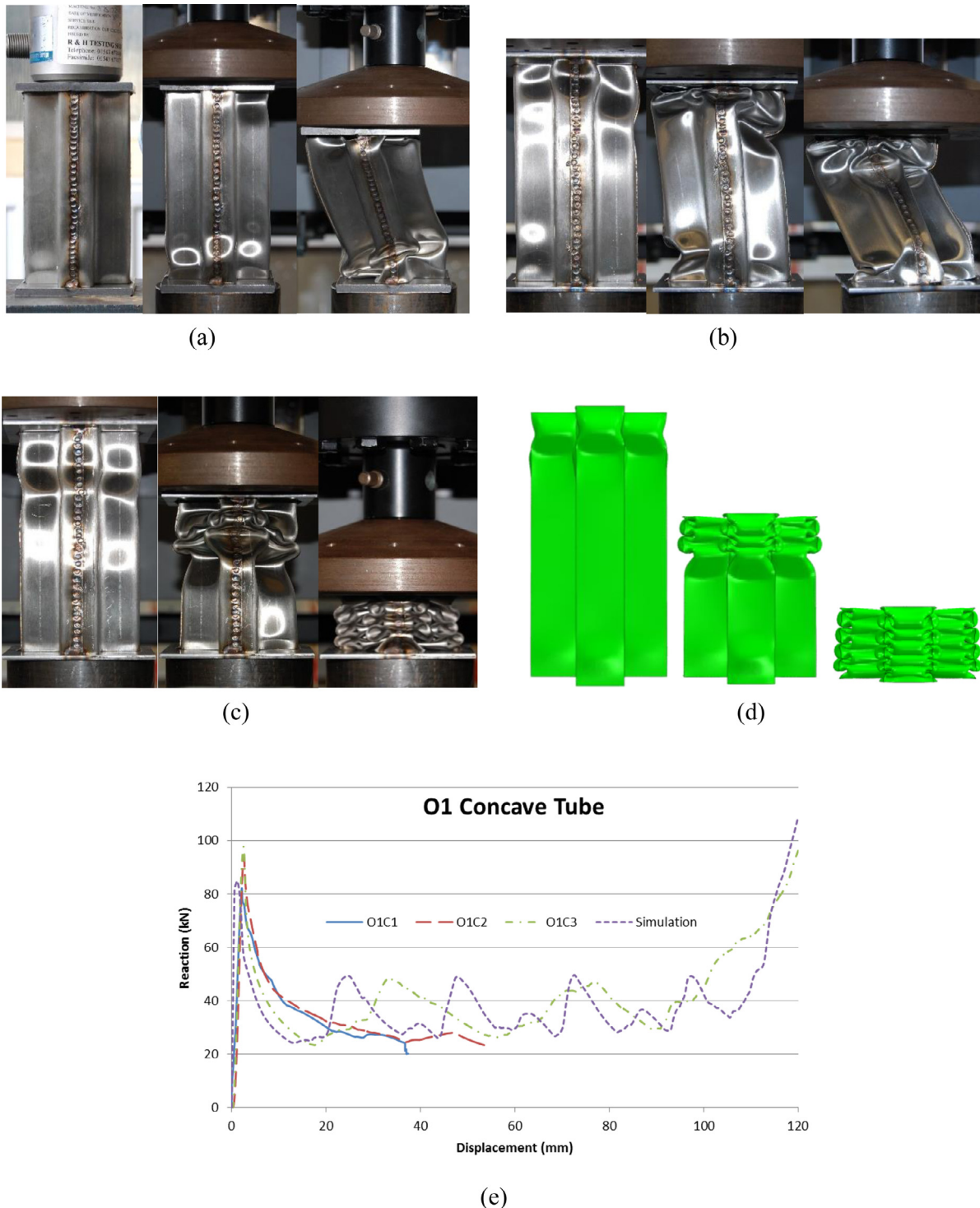


Fig. 9. Experimental crushing of: (a) O1C1 by the hydraulic and Instron machines in sequence, with displacements of 3 mm, 6.3 mm, and 39.3 mm; (b) O1C2 by Instron machine with displacements of 3.3 mm, 19.8 mm, 52.8 mm; (c) repeated for O1C3; and (d) numerical analysis of the crushing of the O1 concave tube with displacements of 4.8 mm, 60 mm, 110.4 mm; and (e) corresponding reaction-displacement plots.

3.3.4. Crushing of O2 concave tubes

Fig. 11(a) and (b) present the failure modes for O2C1 and O2C2, and Fig. 11(c) shows the failure mechanism for the O2 concave tube in the numerical simulation. All of these deformations resulted in unstable failure modes. O2C1 and O2C2 swayed sideways in an identical fashion when compressed, while the tube in the numerical simulation bulged out in the middle. The reaction-

displacement curves are provided in Fig. 11(d), which shows that all three curves were comparable before being deflected by 20 mm. When the tubes were compressed further, the reaction in the simulation surpassed those in the experiments. This result was due to a different deformation mode occurred in the simulation, which could have provided additional resistance when the middle part of the tube was fully expanded circumferentially. The last deforma-

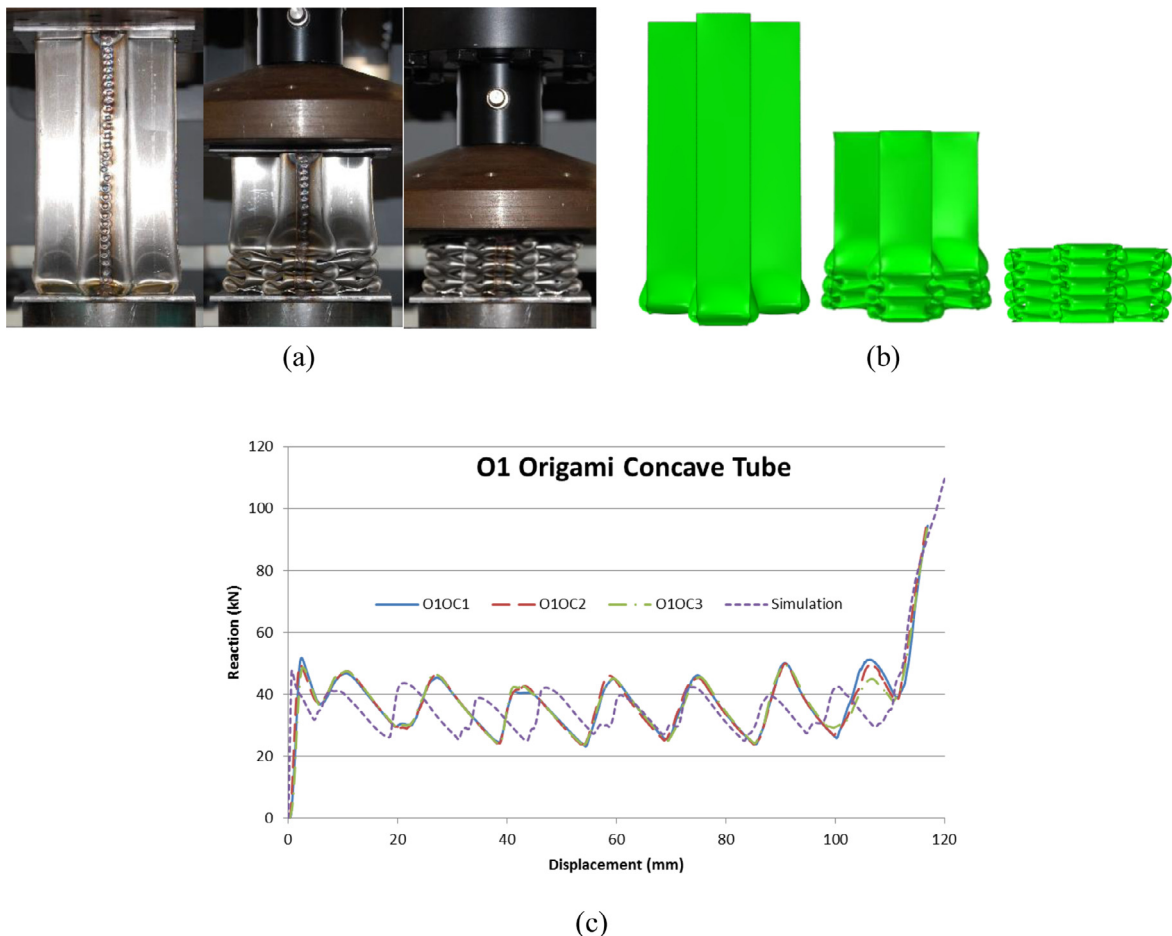


Fig. 10. (a) Experimental crushing of O1OC1 (crushing O1OC2 and O1OC3 resulted in identical failure mechanisms) with displacements of 6 mm, 60 mm, and 114 mm; (b) corresponding numerical simulation; and (c) their reaction-displacement plots.

tion status shown in Fig. 11(c) had a displacement of 20.5 mm, and this status corresponds to the point in Fig. 11(d) at which reactions in the experiment and simulation start to differ.

The failure mode of O2C3 is shown in Fig. 12(a), and the corresponding numerical simulation is shown in Fig. 12(b). Both deformations resulted in unstable buckling and swaying-sideways failure modes. The reaction curves are shown in Fig. 12(c), and the experimental O2C3 had a clearly higher buckling force than the corresponding result in the numerical simulation. This difference could have been caused by the additional connection created between tube and plates in the annealing process (heated up to 1100 °C), which perhaps provided a stronger boundary constraint, leading to a higher buckling force. All of the O2 concave tubes' tests and simulations exhibited non-progressive buckling failures.

3.3.5. Crushing of O2 origami concave tubes

O2OC1, O2OC2, and O2OC3 were compressed in the Instron machine and produced identical progressive failure modes. The deformation of O2OC1 is presented in Fig. 13(a). The numerical simulation for crushing the O2 origami concave tube is given in Fig. 13(b), and its results are comparable to those of the experimental deformations. The reaction-displacement curves are shown in Fig. 13(c). Similar to the case of the O1 origami concave tubes, the reaction curves of the three experimental tubes were the same, but they showed small shifts and slightly lower initial slopes compared to the simulation's curve (Fig. 13(c)).

All crushed samples are presented in Fig. 14. The origami concave tubes appeared to have more intriguing folds of material after being crushed compared to the square and normal concave tubes. Globally unstable failure was dominant in the deformation of the normal concave tubes.

3.4. Discussion

3.4.1. Unstable failure of normal concave tubes

The square tube performed as expected, and its performance was set as the benchmark. Progressive failure occurred, and the tube folded down layer by layer. However, the failure modes of the normal concave tubes were rather inconsistent. O1C3 and the simulation for the O1 concave tube showed progressive buckling, and the rest had non-progressive buckling. A comparison of the simulations for the O1 and O2 concave tubes indicated that the concave tubes with longer relative widths (edge-width divided by thickness) were more likely to buckle progressively. However, even though the O1 concave tubes (with parameters set in this section) had longer relative widths for progressive buckling (as indicated in the simulation), they were sensitive to asymmetry and tended to sway sideways when compressed. This behavior shows that the failure modes of the O1 concave tubes are sensitive to imperfections and not suitable as energy absorbers. For the O2 concave tubes (with parameters set in this section), progressive buckling appeared to be impossible. As a result, both the O1 and O2 concave tubes turned out to be unsuitable for energy absorbing appli-

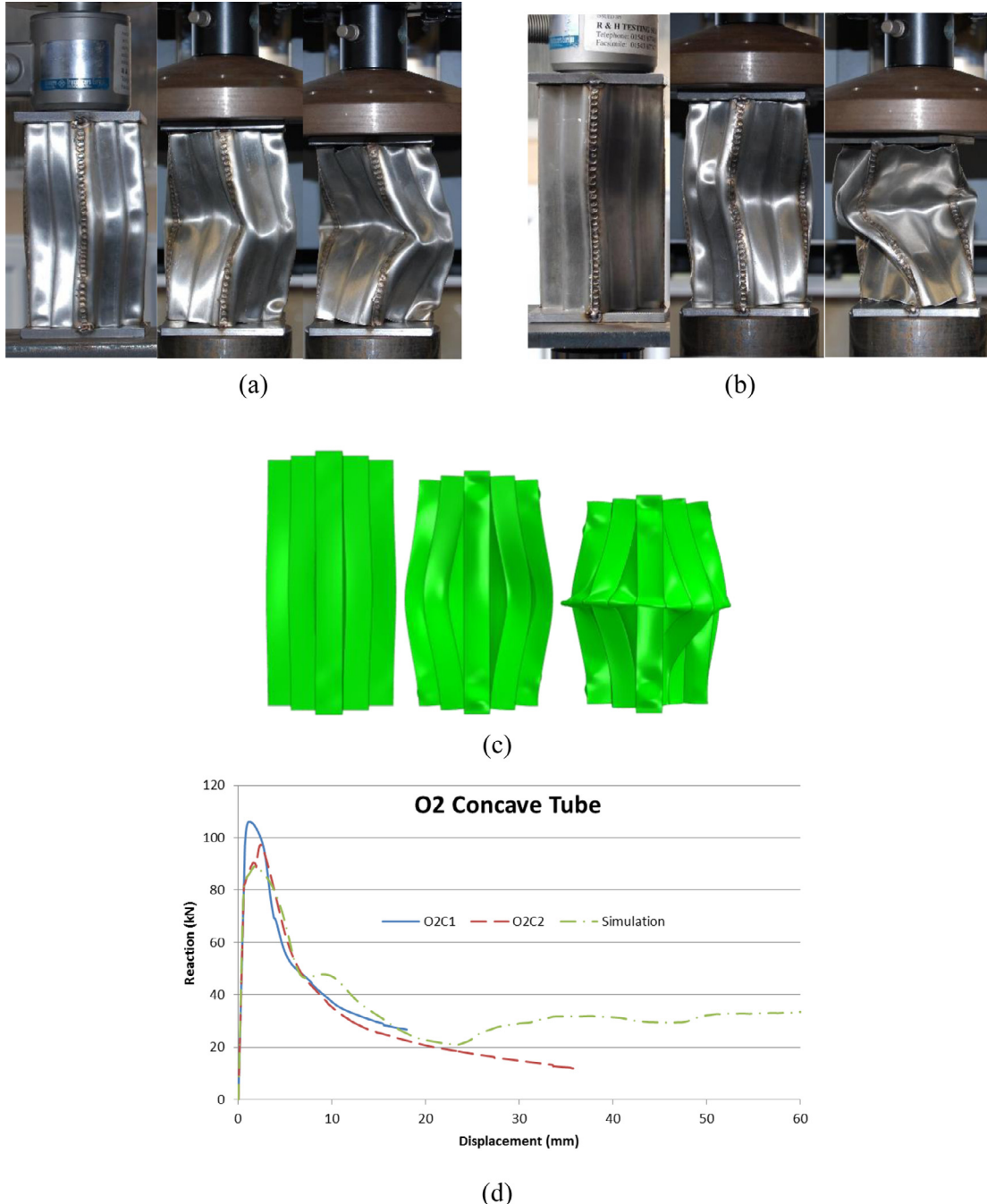


Fig. 11. (a) Crushing of O2C1 by the hydraulic and Instron machines in sequence with displacements of 4 mm, 10.4 mm, and 20.5 mm; (b) crushing of O2C2 via the same method with displacements of 3 mm, 10.4 mm, and 39.3 mm; (c) the numerical simulation with displacements of 2.4 mm, 10.4 mm, and 20.5 mm; and (d) their reaction-displacement plots.

cations due to their high peak forces, non-progressive failure mode, and non-repeatable failure behaviors (Lu and Yu, 2003).

3.4.2. The function of the origami initiator

By introducing origami initiators, the origami concave tubes can buckle progressively and utilize their multi-corner features for high energy absorption. Figs. 10 and 13 show that the origami initiators introduced geometric guidance to the structures, which led the tubes to deform in a designed and geometrically compatible way. It is crucial to add folding to only one layer at one end of the tube, instead of throughout the tube, as Ma and You (Ma and You, 2013) did. When the tube is crushed, the origami initiator will

deform first. While the origami initiator is folding down, it will automatically deform the adjacent layer above it in such a manner as to form another “initiator” layer. This layer will, in turn, form another initiator above it when it is folded down afterwards, and so on in a domino effect. During this entire process, with the exception of the layer folding down currently and its adjacent layer, the upper part of the tube remains straight and rigid. This mechanism brings an order to the crushing process which allows the tube to deform one layer at a time while pre-folding its adjacent layer instead of deforming the tube all at once, causing uncertain and unstable behavior. If origami folding is introduced throughout the tube, as in (Ma and You, 2013), it will behave in the manner

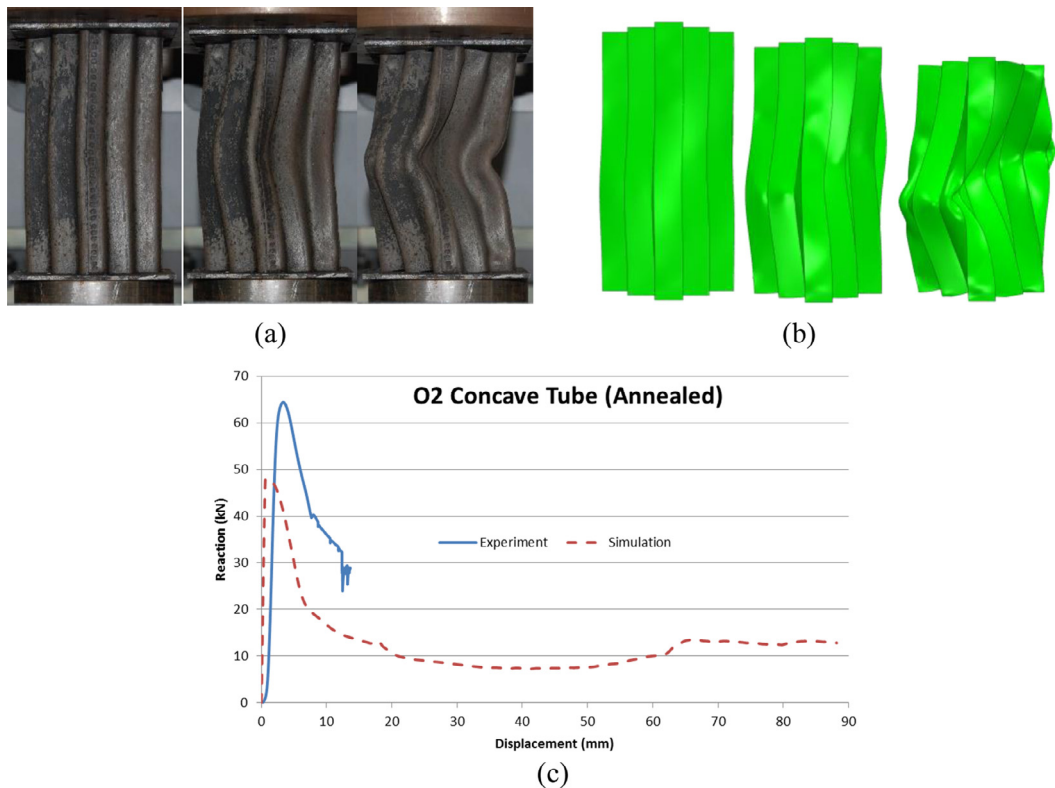


Fig. 12. (a) Crushing of O1C3 by Instron machine with displacements of 2.4 mm, 4.8 mm, and 14.4 mm; (b) the numerical analysis of crushing an O2 concave tube (using annealed 304 stainless steel); and (c) their reaction-displacement curves.

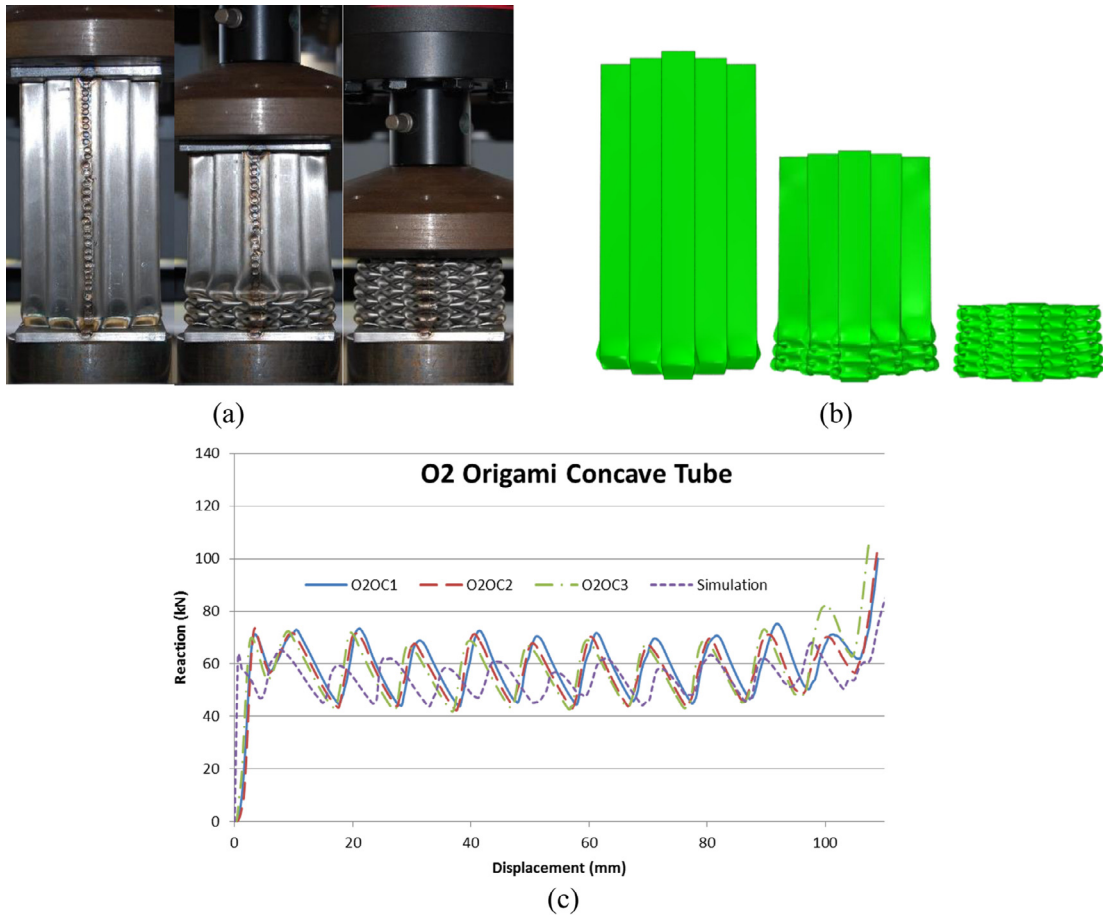


Fig. 13. (a) Experimental crushing of O2OC1 (O2OC2 and O2OC3 produced identical failure mechanisms) with displacements of 2.4 mm, 43.2 mm, and 110.4 mm; (b) corresponding numerical analysis of crushing the O2 origami concave tube; and (c) their reaction-displacement plots.

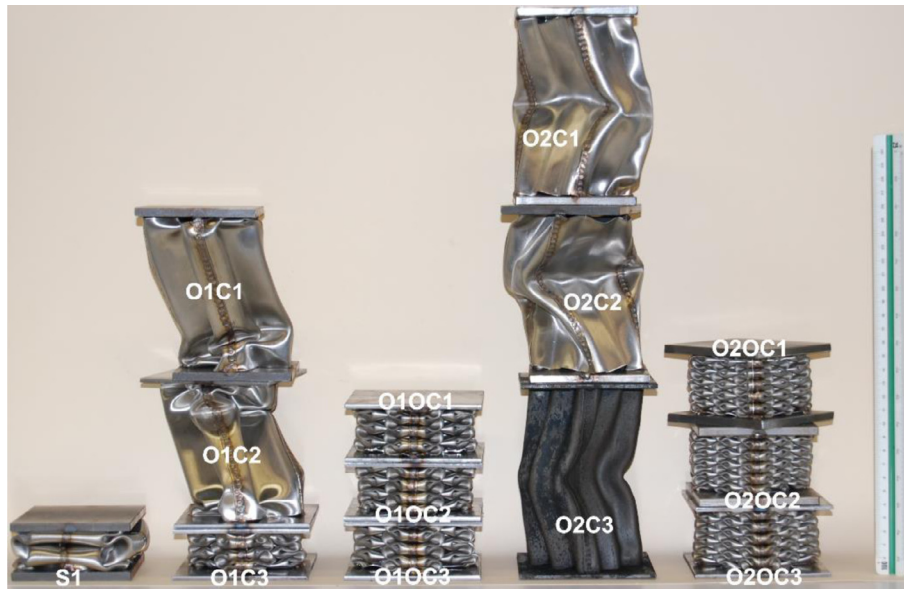


Fig. 14. Crushed samples.

Table 4

Comparison of energy absorbing performance among the square and origami concave tubes.

Type	Peak Force (kN)		Mean Crush Force (kN)		Stroke		Load Uniformity		Mean Crush Force Comparison		SEA (kJ/kg)	
	Exp. (avg.)	FEA	Exp. (avg.)	FEA	Exp. (avg.)	FEA	Exp. (avg.)	FEA	Exp. (avg.)	FEA	Exp. (avg.)	FEA
Square Tube	41.5	32.4	18.2	14.1	78.2%	80%	2.28	2.31	—	—	5.47	4.32
O1 origami tube	48.7	47.3	36.5	34.4	75.2%	74.8%	1.33	1.38	200.5%	244.0%	10.55	9.88
O2 origami tube	73.0	65.5	58.4	54.4	71.5%	72.4%	1.25	1.20	320.9%	385.8%	16.06	15.14

shown in Figs. 11 and 12 and exhibit a non-progressive buckling mode. Another function of the origami initiator is that it introduces a significant weak layer, making the tube insensitive to small imperfections. Also, the peak reaction force is reduced.

3.4.3. Comparison of the energy absorption of square and origami concave tubes

Due to the undesirable performances of normal concave tubes in terms of energy absorption, the focus of the comparisons is on the square tube and origami concave tubes, as shown in Table 4. Inside the table, "Stroke" is the final crushed length divided by the original length. The final crushed length is measured when the reaction reaches the previous peak force and keeps increasing afterwards. "Load Uniformity" is the ratio between the peak force and the mean crush force. "Mean Crush Force Comparison" is defined as the mean crush force of the origami concave tubes divided by that of the square tube. "SEA" is the ratio between the energy absorption (when deformed to the final crushed length) and mass. The direct plots of the experimental reactions of the origami concave and square tubes are shown in Fig. 15. The origami concave tubes demonstrated that their mean crush forces were several times higher and their load uniformities were significantly lower than those of the square tube. The strokes of the origami concave tubes were reduced slightly compared to the square tube due to the increase in the number of folded layers. This drawback can be solved by introducing tapered shape, and this improvement is presented in Section 7.

A general consistency between the experimental and numerical results was observed. The slight discrepancies observed in terms of the deformation and reaction curves were mainly due to small

Table 5

Comparison of buckling forces between the square tube and the conventional concave tubes.

Type	Peak Force (kN)		Comparison	
	Exp.	FEA	Exp.	FEA
Square Tube	41.5	32.4	—	—
O1 concave tube	97.8	84.9	235.7%	262.0%
O2 concave tube	105.8	89.2	254.9%	275.3%

manufacturing imperfections, the sensitive features of samples, and machine compliance, all of which were not technical mistakes and were practically tolerable. These results indicate that further studies can rely on numerical analyses.

3.4.4. Approaching the theoretical limit of energy absorption

The O1 and O2 concave tubes have ultra-high buckling forces, as shown in Table 5. In Table 5, the values under the "Comparison" heading are calculated as the peak force of a concave tube divided by that of the square tube. From the table, it can be seen that the buckling forces have been more than doubled by introducing concave cross-sections. However, when adding more corners by following the trend in Fig. 16, the buckling force cannot increase in an unlimited fashion, while the increase in the mean crushing force corresponding to the progressive failure mode has no limit. This will lead to a critical point at which the mean crushing force almost reaches the buckling force, i.e., the theoretical limit for energy absorption. The O2 origami concave tube presented here is close to that optimal case. This point is illustrated further in Section 5.4.

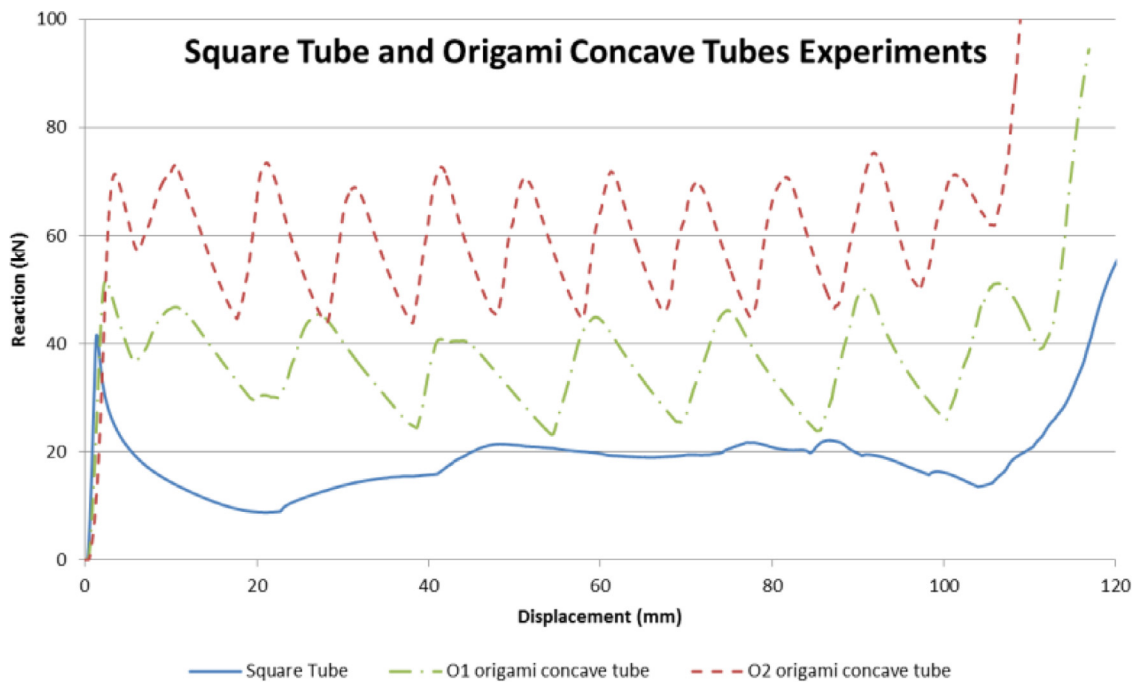


Fig. 15. Plot of the reaction forces of the square and origami concave tubes from the experiment.

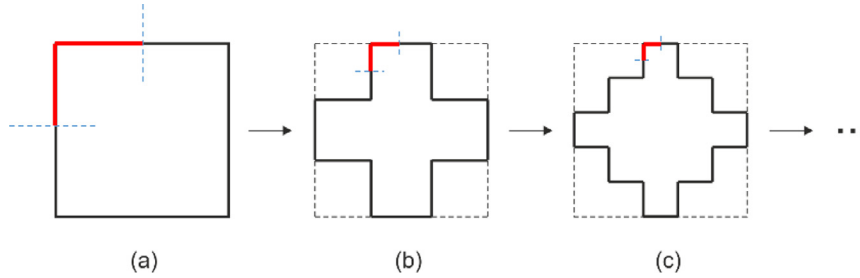


Fig. 16. Shape changes from square to concave.

4. Theoretical modeling

In order to enable a quick estimation of the energy absorption of origami concave tubes to assist future design, simple theoretical models of origami concave tubes are introduced in this section.

First, let us consider one element of a basic failure pattern, the idealized collapse mechanism, which is shown in Fig. 17(a). This sketch is for one corner of an origami concave tube, and a repetitively folded element of it is shown in Fig. 17(b). The mean crush

force P_m of a square tube with a symmetric buckling mode based on this element can be expressed by (Wierzbicki and Abramowicz, 1983)

$$P_m = 9.56\sigma_0 t^{\frac{5}{3}} c^{\frac{1}{3}}, \quad (1)$$

where σ_0 is the plastic flow stress of the material, t is the wall thickness, and c is the length of (AB + BC) in Fig. 17(a). Considering that an effective crushing length is about 70% of the total length of the tube (Abramowicz, 1983), the P_m of the square tube can be

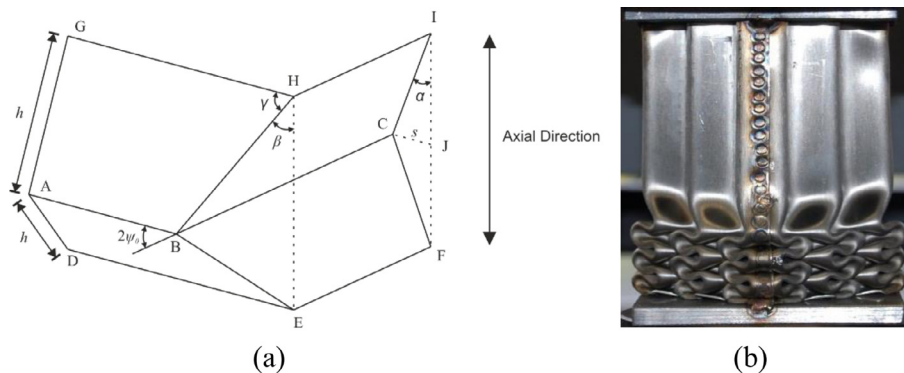


Fig. 17. Tube crushing mechanism. (a) Idealized collapsing mechanism of one corner, and (b) collapse mode of an O2 origami concave tube.

Table 6

Comparison of theoretical results with experimental and numerical results.

Type	Mean Crush Force				Number of Folds			
	Exp. (kN)	FEA (kN)	Theoretical (kN)	Theoretical to FEA Difference		Exp.	FEA	Theoretical
Square Tube	18.2	14.1	16.3	15.6%	3	4	4.44	11.1%
O1 origami tube	36.5	34.4	33.9	-1.5%	7	9	9.25	2.70%
O2 origami tube	58.4	54.4	47.7	-12.3%	10	12	12.99	8.27%

rewritten as

$$P_m = 13.66\sigma_0 t^{\frac{5}{3}} c^{\frac{1}{3}}. \quad (2)$$

The length h (noted in Fig. 17(a)) of each layer can be expressed as (Wierzbicki and Abramowicz, 1983)

$$h = 0.983^3 \sqrt{tc^2}. \quad (3)$$

The buckling of origami concave tubes follows the same basic mechanism that the square tube does but undergoes more repetitions. One corner of the square, O1 origami, and O2 origami tubes is marked red respectively in Fig. 16. Based on Eq. (2), the P_m of one corner (1/4 of a square) is $\frac{13.66}{4} \times 2^{\frac{1}{3}} \times \sigma_0 t^{\frac{5}{3}} w_0^{\frac{1}{3}}$, where $w_0 (=c/2)$ is the width of one flange for one corner. An O1 origami tube has 12 such corners (including 4 reflex corners which have the same failure mechanism), and the width of the tube (c) is 6 times the width of one corner flange. Thus, its mean crush force is

$$P_{m1} = \frac{13.66}{4} \times 2^{\frac{1}{3}} \times 12 \times \frac{1^{\frac{1}{3}}}{6} \sigma_0 t^{\frac{5}{3}} c^{\frac{1}{3}} = 28.42\sigma_0 t^{\frac{5}{3}} c^{\frac{1}{3}}. \quad (4)$$

Similarly, the mean crush force for an O2 origami concave tubes can be expressed as

$$P_{m2} = \frac{13.66}{4} \times 2^{\frac{1}{3}} \times 20 \times \frac{1^{\frac{1}{3}}}{10} \sigma_0 t^{\frac{5}{3}} c^{\frac{1}{3}} = 39.94\sigma_0 t^{\frac{5}{3}} c^{\frac{1}{3}}, \quad (5)$$

where c equals $3w$ and $5w$ for the O1 and O2 origami tubes respectively. It is also equal to one-fourth of the cross-sectional circumference. Their corresponding lengths for each layer during crushing are

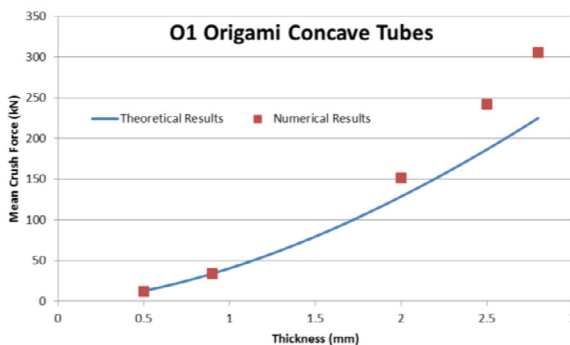
$$h_1 = 0.983^3 \sqrt{t \left(\frac{c}{3}\right)^2} = 0.473 \sqrt{tc^2} \quad (6)$$

and

$$h_2 = 0.983^3 \sqrt{t \left(\frac{c}{5}\right)^2} = 0.336 \sqrt{tc^2}. \quad (7)$$

The equivalent plastic flow stress σ_0 can be calculated by (Ma, 2011)

$$\sigma_0 = \sqrt{\frac{\sigma_y \sigma_u}{1 + n_s}}, \quad (8)$$



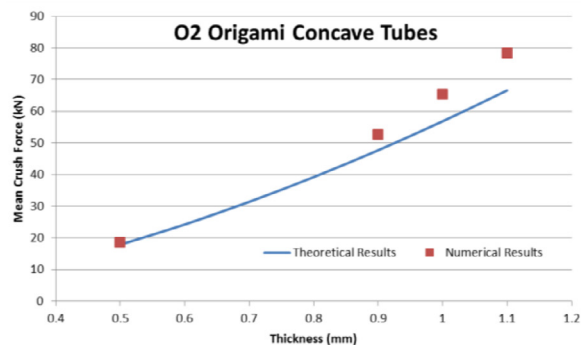
(a)

where n_s is the strain hardening exponent, which equals 0.43 for 304 stainless steel.

Eqs. (2), (4) and (5) provide estimates of the mean crush force for the square, O1 origami, and O2 origami concave tubes, respectively. Putting the parameters of the tubes which were tested and simulated in Section 3 into these models results in the mean crush forces of the square, O1 origami, and O2 origami tubes being 16.3 kN, 33.9 kN, and 47.7 kN, respectively. Eqs. (3), (6), and (7) provide the number of folds for those tubes, which turn out to be 4.44, 9.25, and 12.99 for the square, O1 origami, and O2 origami tubes, respectively. A comparison of the theoretical with the experimental and numerical results is shown in Table 6, and the theoretical values are fairly consistent with those obtained via experiment and simulation. Compared to the numerical results, the theoretical results overestimate the mean crush force for the square tube and underestimate it for the O2 origami tube. One of the possible reasons for this outcome could be that the theoretical model assumes a 70% stroke for all situations. However, a smaller w/t value leads to more folded layers, which might result in a smaller stroke than a constant 70%. Models with a more realistic estimate of the effective crushing distance need to be developed in the future. A series of numerical simulations have been run with different wall thicknesses for the origami concave tubes, and a comparison of the results with the results of Eqs. (4) and (5) is shown in Fig. 18. The theoretical model matches the numerical results well when t is smaller, while it underestimates the mean crush forces slightly for larger t .

These simple theoretical models can provide a quick and conservative estimation of the energy absorbing capacity of origami concave tubes, which shall be very useful for preliminary designs. Eqs. (4) and (5) suggest that the mean crushing forces for the O1 and O2 origami concave tubes are, respectively, 2.1 and 2.9 times that of the square tube (Eq. (2)). Simple geometric optimization can be done by dividing Eqs. (4) or (5) by $t \cdot c$, which is an expression for the cross-sectional area. This will give us a ratio (after neglecting the constants) of

$$\frac{P_m}{m} = s \cdot \left(\frac{t}{c}\right)^{\frac{2}{3}}, \quad (9)$$



(b)

Fig. 18. Plots of the theoretical and numerical results for the (a) O1 and (b) O2 origami concave tubes.

Table 7

Parametric study of O1 origami concave tube.

w/t ratio	l/w	α (°)	l_2 (mm)	Buckling load of concave tube	Peak reaction of origami concave tube	Differential ratio	Failure mode
50	6	80.66	7.5	39.9	17.5	2.29	Progressive
27.78	6	80.66	7.5	90.1	47.3	1.91	Progressive
12.5	6	80.66	7.5	260.6	198.3	1.31	Progressive
10	6	80.66	7.5	348.2	283.9	1.23	Progressive
8.93	6	80.66	7.5	401.3	357.2	1.12	Progressive
8.33	6	80.66	7.5	437.3	401.0	1.09	Mixed
7.81	6	80.66	7.5	473.8	443.2	1.07	Non-progressive
10	10	80.66	7.5	–	–	–	Progressive
10	12	80.66	7.5	–	–	–	Progressive
10	14	80.66	7.5	–	–	–	Progressive
10	6	60	7.5	–	–	–	Progressive
10	6	85	7.5	–	–	–	Progressive
10	6	85	$h_1/2 = 5$	–	–	–	Non-progressive
10	6	85	$2/3h_1=7.5$	–	–	–	Progressive
10	6	85	$2h_1=23$	–	–	–	Progressive

Table 8

Parametric study of O2 origami concave tube.

w/t ratio	l/w	α (°)	l_2 (mm)	Buckling load of concave tube	Peak reaction of origami concave tube	Differential ratio	Failure mode
30	10	80.66	7.5	45.3	26.8	1.69	Progressive
16.67	10	80.66	7.5	89.5	69.0	1.30	Progressive
15	10	80.66	7.5	99.7	82.7	1.21	Progressive
13.64	10	80.66	7.5	109.9	95.3	1.15	Progressive
12.5	10	80.66	7.5	120.9	108.8	1.13	Mixed
11.54	10	80.66	7.5	141.2	123.8	1.14	Mixed
10.71	10	80.66	7.5	153.4	140.0	1.10	Non-progressive
15	12	80.66	7.5	–	–	–	Progressive
15	13.3	80.66	7.5	–	–	–	Non-progressive
15	10	60	7.5	–	–	–	Progressive
15	10	85	7.5	–	–	–	Progressive
15	10	85	$h_2/2 = 3$	–	–	–	Non-progressive
15	10	85	$2/3h_2=6$	–	–	–	Progressive
15	10	85	$2h_2=12$	–	–	–	Progressive

Table 9

Preferred range of parameters.

Types	w/t	l/w	α (°)	l_2
O1 origami concave tube	≥ 10	≤ 12	$60 \sim 85$	$2/3 h_1 \sim 2 h_1$
O2 origami concave tube	≥ 15	≤ 12	$60 \sim 85$	$2/3 h_2 \sim 2 h_2$

where m is the mass of the tube, and s is a constant. Eq. (9) suggests that relatively thicker material can increase the energy absorption per unit mass (SEA). However, this conclusion might not hold if tubes buckle in different ways. In consequence, it is crucial to guarantee that the progressive failure modes (in Figs. 10 and 13) occur through the appropriate selection of parameters, which is studied next in Section 5.

5. Parametric study

The progressive buckling of origami concave tubes provides good energy absorption. However, non-progressive buckling (such as in Fig. 11) can occur in origami concave tubes if the parameters are not appropriate. The purpose of the parametric study in this section is to discover the appropriate ranges for these parameters in order to guarantee the progressive buckling of the origami concave tubes. Our study relies on a numerical analysis which has the same settings in terms of mesh density, material, and so on as found in Section 3. The results of the parametric study are presented in Tables 7 and 8 for the O1 and O2 origami concave tubes, respectively, and preferred ranges of parameters are given in Table 9 for design guidance. The different aspects of the parametric effects are discussed below.

5.1. Effect of the w/t ratio and tube length l

The successful crushing of an origami concave tube requires that the buckling force of the concave tube (without the origami initiator) to be sufficiently larger than the reaction needed for the progressive failure of its origami version. The buckling force for the O1 and O2 concave tubes will be proportional to $t^2(\frac{w}{t})^{m_1}$ (Timoshenko, 1961), and the mean crush force of the origami concave tubes will be proportional to $t^2(\frac{w}{t})^{m_2}$, as indicated in Section 4, where m_1 and m_2 are the corresponding exponents. The result of dividing the first expression by the second should be considerably larger than 1 in order for the progressive failure to occur, and this product is only associated with w/t .

With this understanding, a series of numerical simulations with different w/t ratios of O1 and O2 origami concave tubes were run, and the results are shown in Tables 7 and 8. Inside the tables, the differential ratio refers to the buckling load of the concave tube divided by the peak reaction of the origami concave tube. This ratio should be considerably larger than 1 to enable a progressive failure mode. Failure modes are categorized as progressive, mixed, and non-progressive. These two tables show that relatively thicker origami tubes can suffer from non-progressive buckling again. The geometries of the tubes are the same as they were in Table 1, with the exception of the thickness. Further, the settings used in the numerical simulations are the same as they were in Section 3, with the exception of the fully clamped boundary condition. The failure modes of the O1 origami concave tubes with w/t ratios of 8.93, 8.33, and 7.81 are shown in Fig. 19. The failure modes of the O2 origami concave tubes with w/t ratios of 13.64, 11.54, and 10.71 are shown in Fig. 20. From these figures, it can be seen that the failure modes change from progressive to non-progressive as the w/t

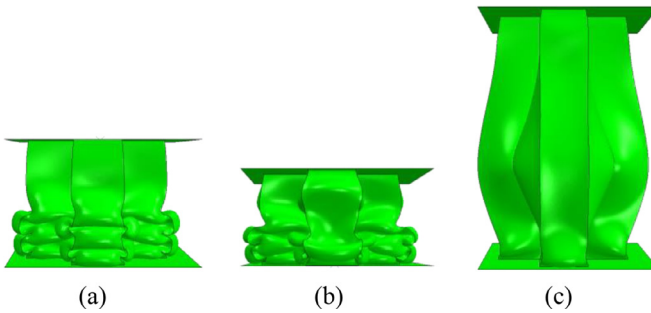


Fig. 19. Deformation of crushing of O1 origami concave tubes with w/t ratios of (a) 8.93, (b) 8.33, and (c) 7.81.

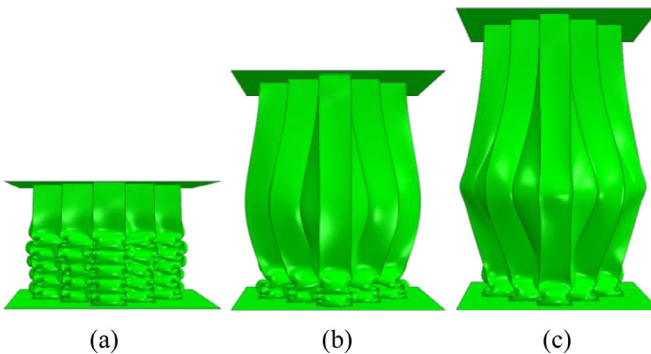


Fig. 20. Crushing of O2 origami concave tubes with w/t ratios of (a) 13.64, (b) 11.54, and (c) 10.71.

ratio decreases. The change in the peak forces of the tubes and the differential ratios, which occur with changing values of w/t , have been plotted in Fig. 21. The figure shows that thinner tubes have a larger differential ratio between the peak force of the concave tube and the corresponding origami concave tube, i.e., they are more likely to achieve progressive buckling modes. The switching points for the O1 and O2 origami concave tubes from progressive to non-progressive are at $w/t = 8.93$ and 13.65, respectively. For conservatism, the working zone for w/t has been chosen as $w/t > 10$ for O1 origami tubes, and $w/t > 15$ for O2 origami tubes, as shown in Table 9.

The increase in l , which is the total length of the tube, will also increase the possibility of unstable behavior of the origami concave tubes. A numerical analysis has been done for the O1 and O2 origami tubes with different values of l , and the results are also presented in Tables 7 and 8, respectively. These results show that the O1 origami concave tubes had progressive failures at

$l = 350$ mm and the O2 origami concave tubes could maintain progressive deformations for the values of l smaller than 180 mm. The deformations resulting from crushing O1 origami concave tubes ($l = 350$ mm) and O2 origami concave tubes ($l = 180$ and 200 mm) are shown in Fig. 22. The O1 origami concave tubes demonstrated progressive failure throughout. When l was increased to 200 mm, the O2 origami concave tube bulged out. In consequence, it is conservatively recommended that l/w shall be smaller than 12 for both O1 and O2 origami concave tubes, as shown in Table 9.

5.2. Design of the origami initiator

The geometry of origami initiator is controlled by two parameters, α and l_2 , as shown in Fig. 2. The value of l_2 was initially set as 7.5 mm, α was altered to 60° and 85° , and all tubes exhibited a progressive failure mechanism. In order to discover the limit of l_2 , α was set as 85° , and l_2 was altered from $h/2$ to 2 h (h can be calculated from Eqs. (6) and (7)). It was found that conservative range of l_2 is from $2/3 h$ to 2 h. The non-progressive failure modes of the O1 and O2 origami concave tubes with l_2 values of 5 mm and 3 mm, respectively, are shown in Fig. 23.

5.3. Imperfection and boundary condition sensitivity

Thinner tubes (with larger w/t ratios) are more sensitive to geometric imperfections (Jones, 2006). An imperfection with an amplitude of 0.5 mm was added to tubes with the same geometry shown in Table 1, with the exception of the 0.5 mm wall thickness. Both tube types exhibited stable progressive failure and demonstrated their low imperfection sensitivity, as shown in Fig. 24. This is because the origami initiator and the corresponding domino effect are more dominating than the superposed imperfections.

In order to observe the effects of different practical boundary conditions, some tubes were partially clamped, as shown in Fig. 7, and other tubes were fully clamped at two ends. The geometries of all tubes were the same as presented in Table 1. The tubes showed identical deformations, and the comparison of their reaction forces is shown in Fig. 25. These results show that changing the boundary conditions does not change the performance of the tubes, except for a slight shift in the phase of the reaction curve.

In conclusion, origami concave tubes are not sensitive to practical imperfections and boundary conditions.

5.4. Summary of design parameters

After running a series of simulations with different parameters, the valid range of these parameters were worked out, as shown in

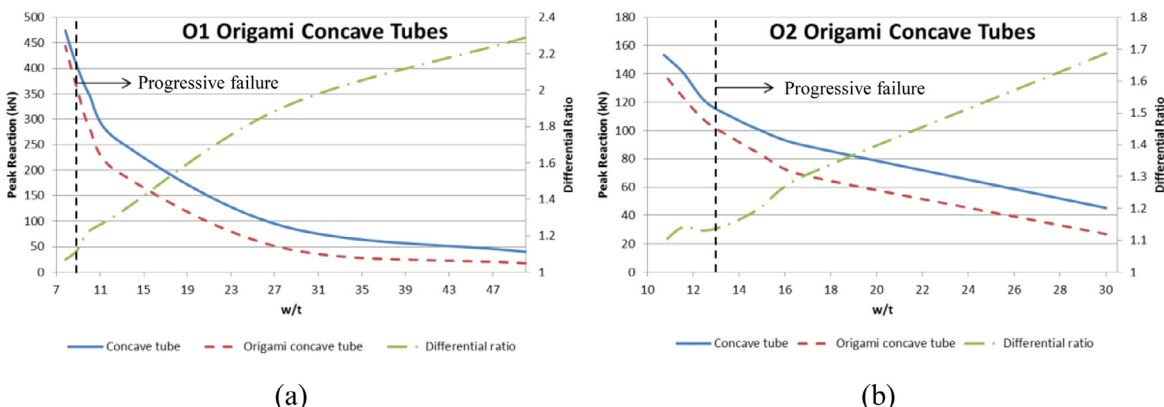


Fig. 21. Changes in peak forces and differential ratios with changing values of w/t for (a) O1 and (b) O2 origami concave tubes.

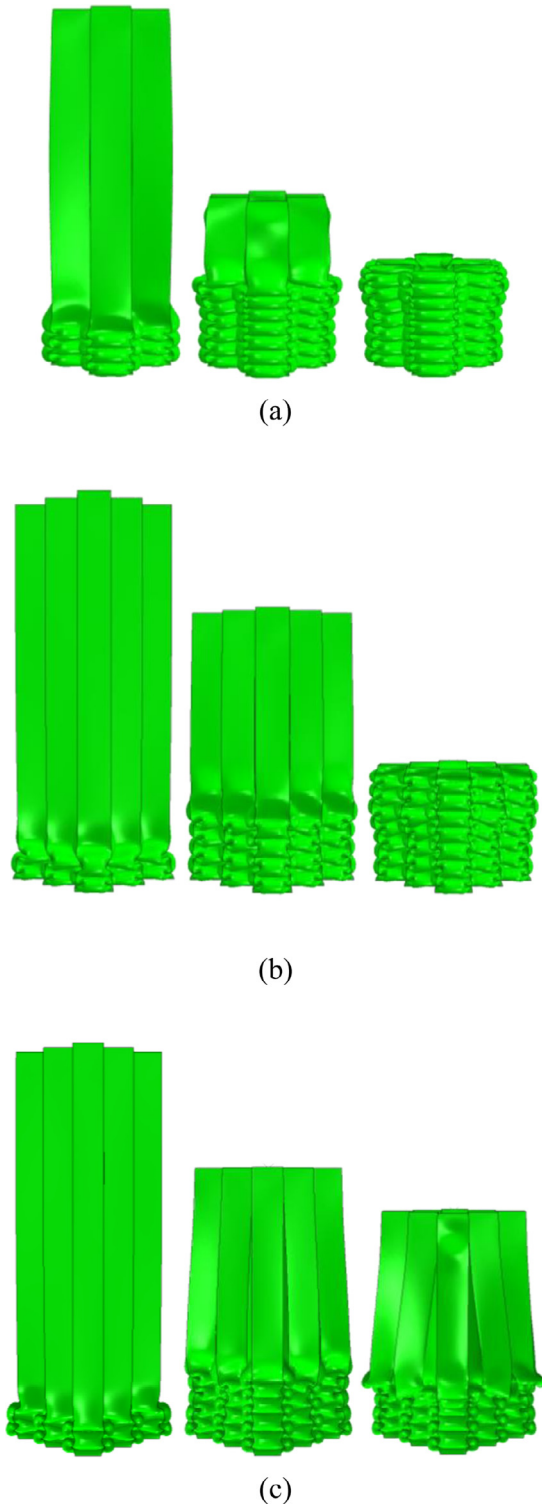


Fig. 22. Deformations of O1 and O2 origami concave tubes with different tube lengths: (a) length is 350 mm, and displacements are 120 mm, 240 mm, and 285 mm, respectively; (b) length is 180 mm, and displacements are 30 mm, 75 mm, and 132 mm, respectively; (c) length is 200 mm, and displacements are 34 mm, 85 mm, and 102 mm, respectively.

Table 9. Staying within these ranges guarantees the stable progressive failure mechanism of origami concave tubes. The performance of origami concave tubes is not sensitive to practical geometric imperfection and boundary conditions. Within the range given in **Table 9**, a smaller w/t ratio will provide higher energy absorption per unit mass.

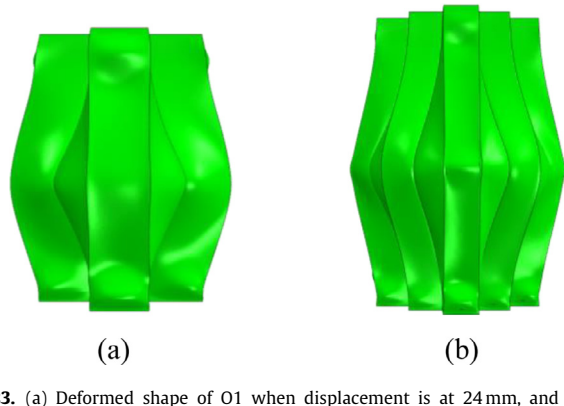


Fig. 23. (a) Deformed shape of O1 when displacement is at 24 mm, and (b) deformed shape of O2 when displacement is at 12 mm.



Fig. 24. Deformation of crushing the imperfect (a) O1 origami concave tube and (b) O2 origami concave tube.

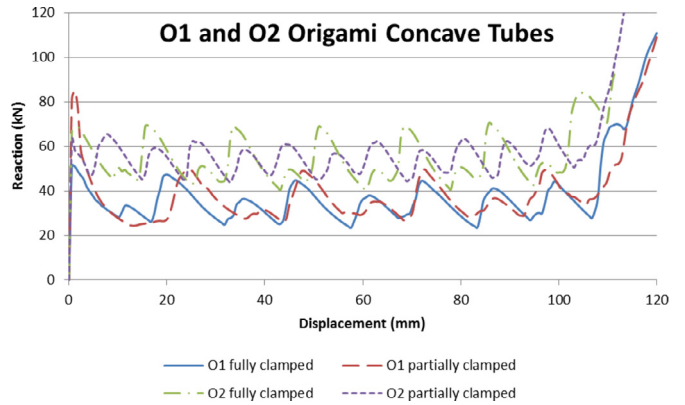


Fig. 25. Reaction-displacement plots for O1 and O2 origami concave tubes with different boundary conditions.

Tables 7 and **8** show that, when w/t decreases, the load required for the progressive buckling of origami concave tube gets close to the buckling load of its corresponding concave tube (differential ratio close to 1). Considering another aspect, the buckling force of the concave tubes with relatively short widths is almost the highest (as illustrated in **Table 5**) among different cross sections (Fan et al., 2013; Ning and Pellegrino, 2015). In other words, concave tubes are providing nearly the largest peak reaction force. In consequence, due to the low load uniformity, the origami concave tubes are absorbing energy with a mean crush force that is close to the peak buckling force of concave tubes. That is to say, origami concave tubes are among the most efficient energy absorbers, in theory.

6. Dynamic and inclined loading

In order to discover the effects of dynamic and inclined loading, tubes with the parameters listed in **Table 10** were chosen for simulation. These parameters are close to the limits suggested in **Table 9**, thus providing tubes with the most unstable performances and sensitivity to dynamic and inclined loadings.

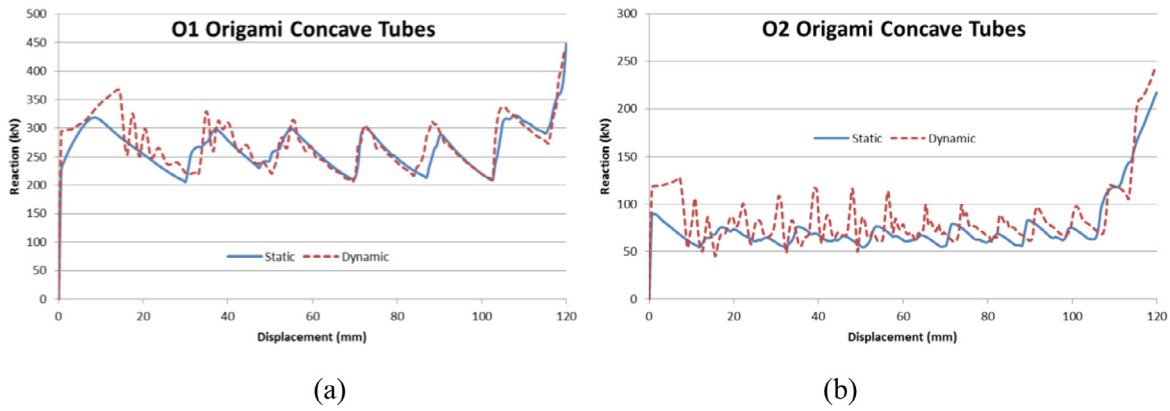


Fig. 26. Reaction-displacement plots for static and dynamic loading of (a) O1 and (b) O2 origami concave tubes.

Table 10
Parameters chosen for simulation.

Types	w/t	l (mm)	α ($^{\circ}$)	l_2
O1 origami concave tube	10	150	85	2/3 h_1
O2 origami concave tube	15	150	85	2/3 h_2

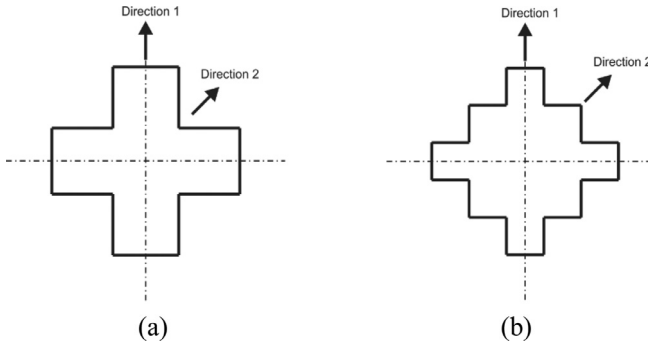


Fig. 27. Defining directions 1 and 2 for (a) O1 and (b) O2 origami concave tubes.

6.1. Dynamic loading

The settings for the simulation were as given in Section 5.1, except the speed of displacement was changed to 30 m/s (120 mm in 0.004 s). A comparison of the static and dynamic cases in terms of the reaction is shown in Fig. 26. This figure shows that there were stress waves transmitting through the structures, which generated more fluctuations in the reaction force. The failure mechanisms of static and dynamic cases were identical, and the ratio of kinematic to internal energy was still well below 5%. Based on these results, it can be concluded that dynamic loading (at middle speed) has no obvious effect on the failure mechanism and only produces a slight change in the reaction force.

6.2. Inclined loading

Inclined displacements with angles of 5° and 10° were applied, respectively. Two directions of inclination were defined, direction 1 and 2, as shown in Fig. 27. Deformations are shown in Fig. 28, and plots are shown in Fig. 29. For the 5° inclination, both origami concave tubes performed almost identically to the performances observed at vertical loading in terms of both failure mechanisms and reaction forces. For the 10° inclination, the failure mechanisms and reaction forces of origami concave tubes changed slightly, but their energy absorbing abilities (mean crush forces) remained the same. From Fig. 29(b), it can be noticed that the inclination of loading,

which enabled accommodation of the material horizontally, could increase the stroke of the O2 origami concave tube. In conclusion, the origami concave tubes can function effectively with inclined loadings (at least within 10° of inclination).

7. Conclusion and future work

Thin-walled tubes with corrugated or concave cross-sections can have ultra-high buckling forces and multiple corners, indicating the potential for high energy absorption. However, their unstable failure modes make them unsuitable for energy absorbing applications as shown in Fig. 30(a). The geometric solution to this issue is to introduce one layer of origami folding at one end of the tube, which works as an initiator in triggering a series of intriguing and progressive folds when compressed, as shown in Fig. 30(b). This simple intervention alters their failure modes from unstable to progressive and realizes their potential for high energy absorption.

This paper has presented this design of origami concave tubes and demonstrated their superior energy absorbing performance compared with the traditional square tube via experimental, numerical and theoretical studies. Specifically, the mean crush force of origami concave tubes is two to four times that of a square tube.

The mean crush force of origami concave tubes can be conservatively estimated by simple theoretical models. Parametric effects related to the failure modes of origami concave tubes have been investigated, and appropriate geometric parameters have been worked out. The theoretical models and suggested range for the parameters given in this paper can provide guidance for a quick preliminary design of origami concave tubes. The performance of an origami concave tube is not sensitive to practical geometric imperfections, boundary conditions, and dynamic and inclined loadings.

A light-weight thin-walled automobile crashcan needs to have a reasonably large cross-section to avoid global buckling and to be as light as possible. In consequence, a structure with a very small wall-thickness that has high energy absorption is needed. The design presented in this paper meets these requirements well. Due to the tremendous increase in energy absorption brought by the origami concave tubes, their application might contribute greatly to lighter-weight vehicles and better protection of passengers during transportation.

In terms of the research on origami concave tubes, future work is required in several areas. First, the effective stroke of theoretical models taking in to account the effect of w/t can be developed. Doing so will lead to more accurate analytical modeling of the energy absorption of origami concave tubes. Theoretical models to evaluate the peak buckling force of concave tubes can be also developed. Such a task was attempted by the authors but not included in this

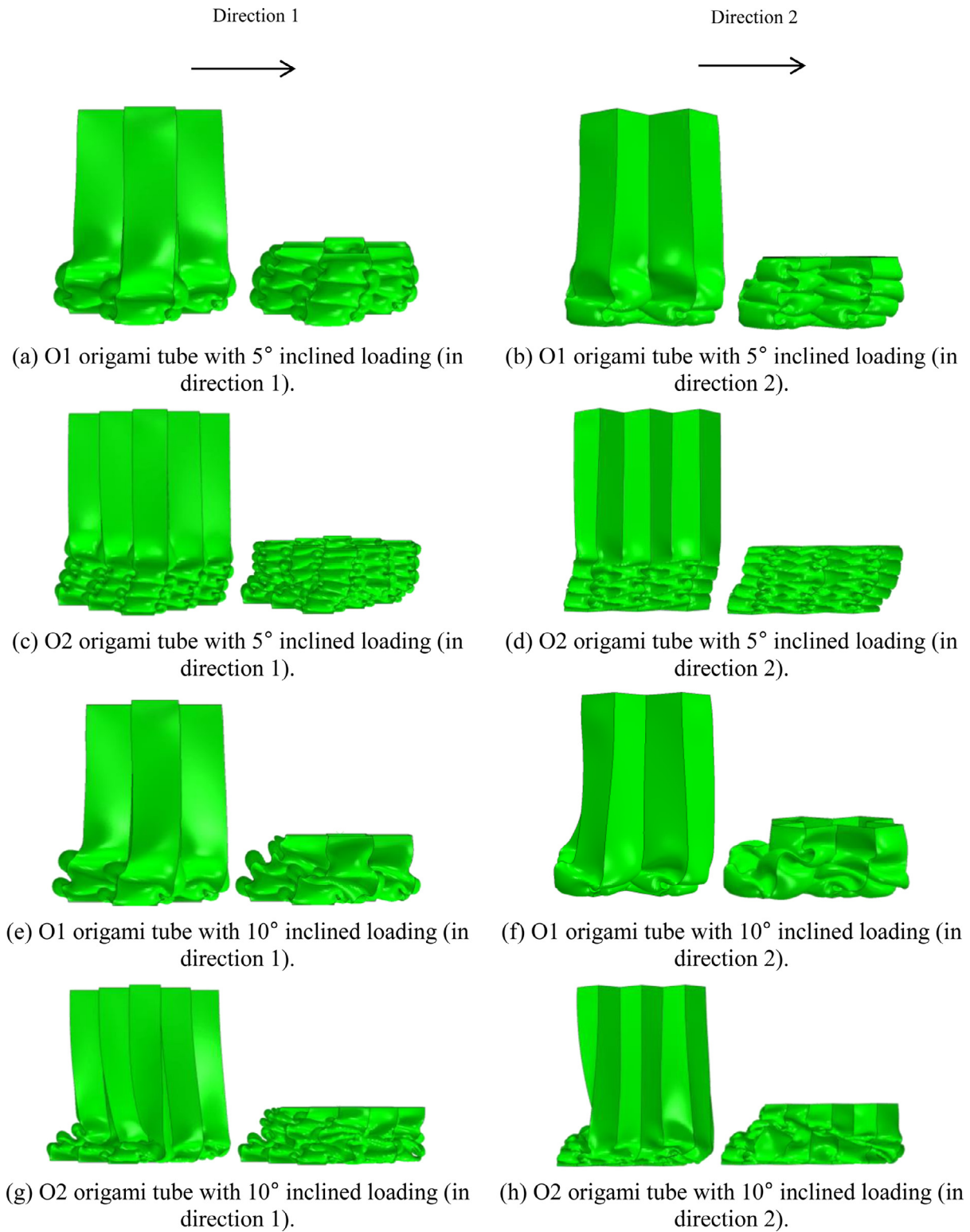


Fig. 28. Deformation of O1 and O2 origami concave tubes under inclined loadings.

paper. This research is greatly meaningful in terms of the design of origami concave tubes. Second, more experiments can be done to confirm the numerical results obtained in the parametric study. Third, further research can be carried out for modified geometries, such as various tapered tubes, tubes with different concave cross sections, and different origami initiators (given in the Appendix). This research direction is illustrated further below.

There are other forms of origami concave tubes that are based on the same concepts. One type of modification is to change the perpendicular shape of the tube into a tapered shape. Another type of modification is to change the cross section into other kinds of concave shapes. Several examples are given below to demonstrate that both directions of modification are effective.

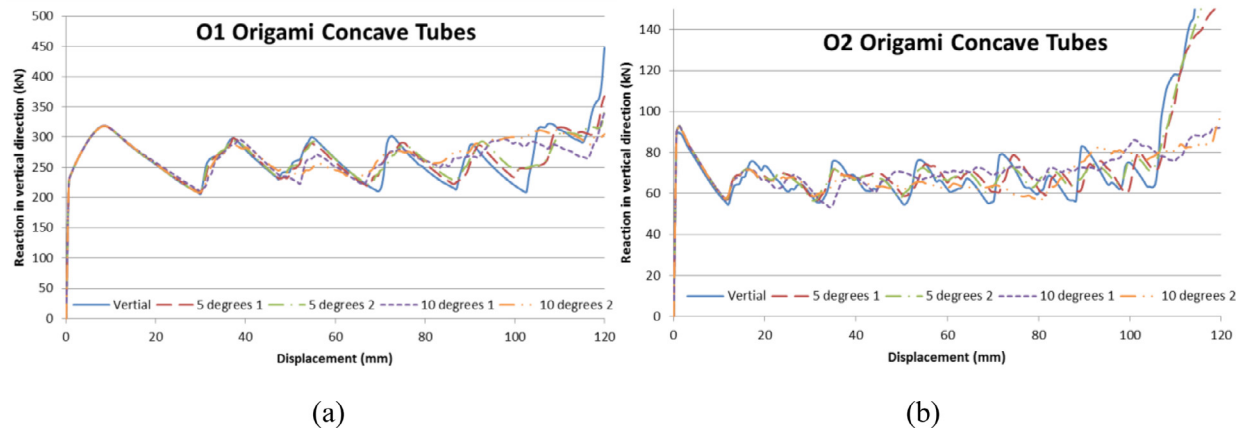


Fig. 29. Reaction-displacement plots for the (a) O1 and (b) O2 origami concave tubes under inclined loadings.

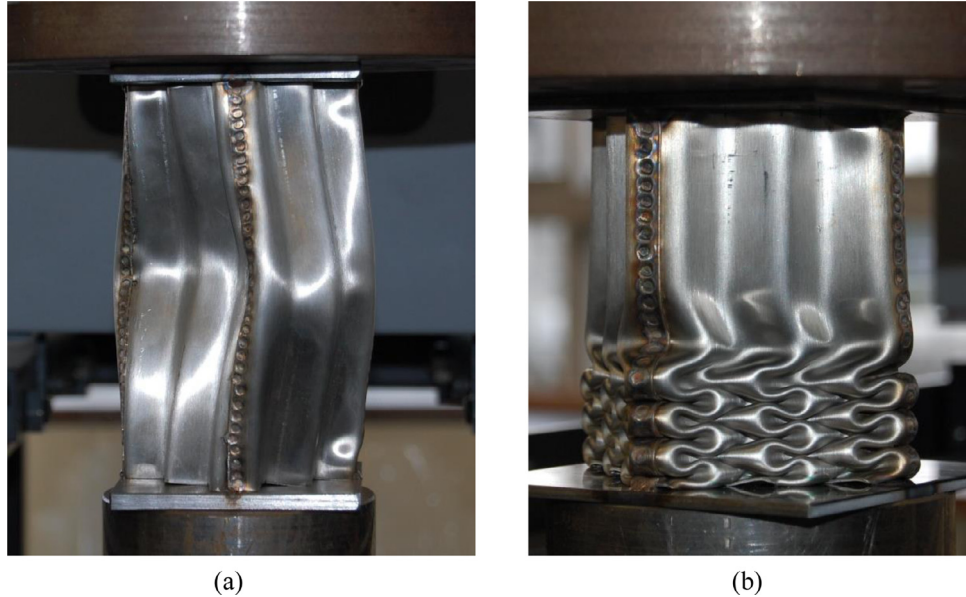


Fig. 30. Experimental failure modes of (a) normal concave tubes and (b) origami concave tubes.

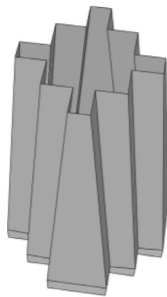


Fig. 31. Geometry of one type of tapered O2 origami concave tube.

7.1. Tapered origami concave tubes

Since the O2 origami concave tube has a reduced stroke, a tapered version can be developed to solve this problem, as shown in Fig. 31. The geometry of the tapered version was modified from the O2 origami concave tube with the parameters outlined in Table 1. A simulation of a tapered tube was done, and its deformation is shown in Fig. 32. The figure shows that the material was not only accommodated vertically but also horizontally, which led to larger stroke, i.e., an increase from 72.4% (perpendicular shape) to 79.3%

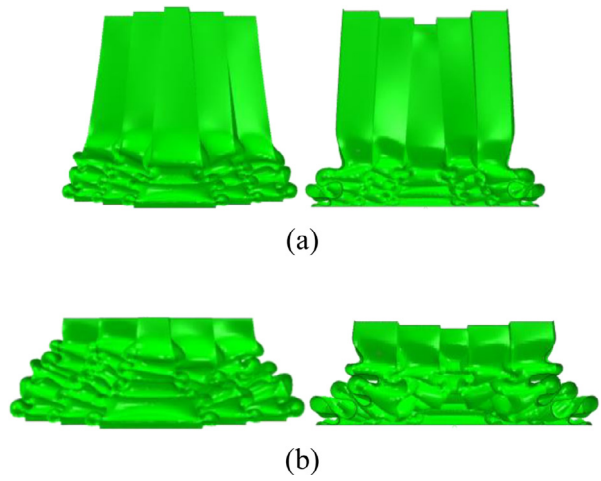


Fig. 32. Deformation of a tapered O2 origami concave tube: (a) when displacement is 60 mm, and its sectional view; (b) when displacement is 108 mm, and its sectional view.

(tapered shape). Different forms of tapered shapes and their corresponding folding patterns are provided in the Appendix.

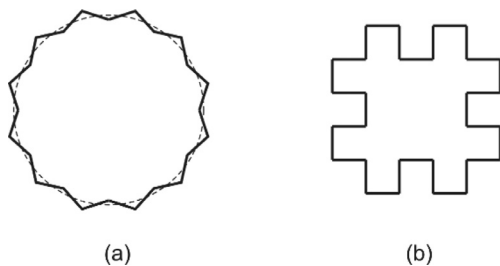


Fig. 33. Two different concave shapes in tube cross-sections.

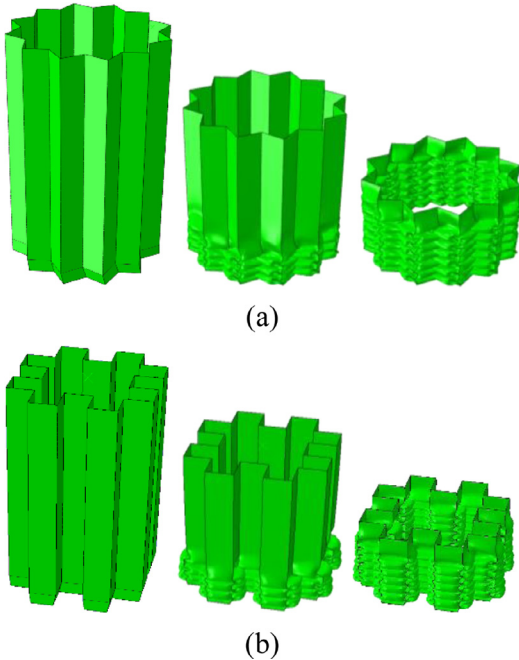


Fig. 34. Deformation of two origami concave tubes with different concave cross-sectional shapes.

7.2. Other concave cross-sections

Further developments based on the previous cross-sections can be achieved by, for example, extending the shape in Fig. 16(c) into an O3 origami concave tube. Beyond focusing on the same base, concave cross-sections from different bases can also be used to develop origami concave tubes based on the same principles. This conclusion was demonstrated with two cross-sections from two different bases, which are shown in Fig. 33. Two corresponding origami concave tubes were made with similar parameters used for the O2 origami concave tubes listed in Table 1. The simulated crushing deformations are shown in Fig. 34, which indicates that they also achieved progressive buckling modes. The geometry

shown in Figs. 33(a) and 34(a) can be used as an alternative to the traditional circular tube. This work demonstrates that the same idea is also applicable to different concave cross-sections. More examples of concave shapes are given in the Appendix. Different cross-sections and configurations might have different features. A comparison of those results can be done to find out more generally optimized designs for different situations, such as for inclined loading and so on.

Acknowledgement

The authors wish to acknowledge the support of the Air Force Office of Scientific Research (FA9550-16-1-0339).

Supplementary material

Supplementary material associated with this article can be found, in the online version, at doi:[10.1016/j.ijsolstr.2019.03.026](https://doi.org/10.1016/j.ijsolstr.2019.03.026).

References

- Abaqus, 2013. Abaqus Documentation Version 6.13. Dassault Systems SIMULIA corp., Providence, RI, USA.
- Abramowicz, W., 1983. The effective crushing distance in axially compressed thin-walled metal columns. *Int. J. Impact Eng.* 1 (3), 309–317.
- Deng, X., Liu, W., Jin, L., 2018. On the crashworthiness analysis and design of a lateral corrugated tube with a sinusoidal cross-section. *Int. J. Mech. Sci.* 141, 330–340.
- DiPaolo, B.P., Tom, J.G., 2006. A study on an axial crush configuration response of thin-wall, steel box components: the quasi-static experiments. *Int. J. Solids Struct.* 43 (25–26), 7752–7775. doi:[10.1016/j.ijsolstr.2006.03.028](https://doi.org/10.1016/j.ijsolstr.2006.03.028).
- Fan, Z., Lu, G., Liu, K., 2013. Quasi-static axial compression of thin-walled tubes with different cross-sectional shapes. *Eng. Struct.* 55, 80–89.
- Jones, R.M., 2006. Buckling of bars, plates, and Shells. Bull Ridge Publishing.
- Li, Y., You, Z., 2018. External inversion of thin-walled corrugated tubes. *Int. J. Mech. Sci.* 144, 54–66. doi:[10.1016/j.ijmecsci.2018.05.044](https://doi.org/10.1016/j.ijmecsci.2018.05.044).
- Liu, S., et al., 2015. Bionic design modification of non-convex multi-corner thin-walled columns for improving energy absorption through adding bulk-heads. *Thin-Walled Struct.* 88, 70–81.
- Liu, W., Lin, Z., Wang, N., Deng, X., 2016. Dynamic performances of thin-walled tubes with star-shaped cross section under axial impact. *Thin-Walled Struct.* 100, 25–37.
- Lu, G., Yu, T.X., 2003. Energy Absorption of Structures and Materials. Elsevier Science.
- Ma, J., 2011. Thin-walled Tubes With Pre-Folded Origami Patterns As Energy Absorption Devices Thesis. University of Oxford.
- Ma, J., You, Z., 2013. Energy absorption of thin-walled square tubes with a prefolded origami pattern—part I: geometry and numerical simulation. *J. Appl. Mech.* 81 (1), 011003–011003.
- Ning, X., Pellegrino, S., 2015. Imperfection-insensitive axially loaded cylindrical shells. *Int. J. Solids Struct.* 62, 39–51.
- Reddy, S., Abbasi, M., Fard, M., 2015. Multi-cornered thin-walled sheet metal members for enhanced crashworthiness and occupant protection. *Thin-Walled Struct.* 94, 56–66.
- Tang, Z., Liu, S., Zhang, Z., 2012. Energy absorption properties of non-convex multi-corner thin-walled columns. *Thin-Walled Struct.* 51, 112–120.
- Timoshenko, S., 1961. Theory of Elastic Stability. McGraw-Hill.
- Weisstein, Eric W. Concave polygon. MathWorld, <http://mathworld.wolfram.com/ConcavePolygon.html>.
- Wierzbicki, T., Abramowicz, W., 1983. On the crushing mechanics of thin-walled structures. *J. Appl. Mech.* 50 (4a), 727–734.